Magnetotelluric source amplitude effect

Xiaoli WAN[1,2*], Hisayoshi SHIMIZU[2], Peng YU[1*], and Hisashi UTADA[2,1]

[1]School of Ocean and Earth Science, Tongji University, Shanghai, China.

[2]Earthquake Research Institute, the University of Tokyo, Tokyo, Japan.

Corresponding authors: Xiaoli WAN (xiaolii.wan@gmail.com) and Peng YU (yupeng@tongji.edu.cn)

Key Points:

- The MT impedance composed of six elements is independent of the source and is a unique response function of the spherical Earth.
- 4-element spherical impedances and tippers are dependent on the source amplitude.
- 4-element and 6-element spherical impedances can be related through tippers.

Abstract

The magnetotelluric (MT) impedances of the three-dimensional (3-D) Earth are typically modelled in a Cartesian coordinate system, ignoring the curvature of the Earth's surface. This approximation is proven to be valid only for the one-dimensional (1-D) Earth. In case of the 3-D Earth, the accuracy of MT impedance estimates derived from Cartesian modeling (Cartesian impedance) must be verified by comparison with estimates obtained reliably using a spherical coordinate system (spherical impedance). While Cartesian impedances under the plane-wave approximation are known to be independent of the source, the influence of the source on spherical impedances remains poorly understood. Therefore, we conducted a systematic study of the source effects on spherical impedances through 3-D modeling for both oceanic and continental regions, employing degree-one sources. Our observations revealed that the source amplitude influences the 4-element spherical impedances and tippers. The 4-element spherical impedance is non-unique, varying with the source amplitude. Tippers are even more significantly and unavoidably affected. To address the non-uniqueness issue of the 4-element impedance, we introduced new impedance elements that incorporate induction by the radial magnetic component, deriving a novel expression for spherical impedance comprising six elements. Numerical experiments demonstrated that the 6-element spherical impedance is uniquely determined (independent of the source amplitude) when three linearly independent sources are provided. Furthermore, we derived a relation between the 6- and 4-element impedances through tippers. The relation not only accounts for the non-uniqueness of the 4-element impedance but may also explain phenomena such as seasonal variations in the impedances.

Plain language summary

This study investigates how to accurately model Earth's properties using the magnetotelluric (MT) method, a geophysical method based on measurements of electric and magnetic fields. This method explores the Earth's electrical structure by modeling the so-called MT impedance, which defines a linear relationship between the two horizontal components of the measured

fields. While modeling in a Cartesian coordinate system has been shown to approximate the Earth effectively in simple one-dimensional models, its reliability becomes questionable when applied to more complex three-dimensional Earth structures. To address this limitation, we conducted a systematic numerical study using a spherical coordinate system, which better accounts for the Earth's curvature. Our results revealed that the amplitude of the source (magnetic disturbances originating in the Earth's ionosphere and magnetosphere) significantly impacts the traditional MT impedance, consisting of four elements, posing challenges in accurately determining Earth's properties. To overcome this issue, we introduced a new MT impedance model consisting of six elements, which establishes a linear relationship between two horizontal electric components and three magnetic components. Numerical experiments demonstrated that this new MT impedance is essentially independent of the source amplitude, offering the potential for improved accuracy in MT modeling and inversion.

1 Introduction

The magnetotelluric (MT) method (Cagniard, 1953) is one of the most effective natural-source electromagnetic (EM) induction techniques. It utilizes the impedance, represented as the complex ratio of horizontal electric to magnetic fields, as a response function that provides information about the Earth's electrical conductivity structure. MT data consist of time series of electric and magnetic fields recorded at an array of observation sites, either on land or the ocean floor. The MT method enables the exploration of depths ranging from the near-surface to several hundred kilometers in the upper mantle. It has been extensively applied in various geophysical investigations, including the petroleum and mineral industries (e.g., Strangway et al., 1973; Livelybrooks et al., 1996; Garcia & Jones, 2000; Jiang et al., 2022), as well as studies of crustal and deep mantle structures (e.g., Stanley et al., 1977; Rosell et al., 2011; Tada et al., 2016; Zhang et al., 2016; Matsuno et al., 2017).

EM induction studies can be broadly classified into two approaches based on the spatial scale of the target and the range of frequencies. The first approach is referred to as global or semiglobal induction studies, in which the Earth is treated as a spherical conductor and the fundamental equation of EM induction is solved in a spherical coordinate system (e.g., Banks, 1969; Schmucker, 1999a, 1999b; Shimizu et al., 2011; Kuvshinov and Semenov, 2012; Grayver et al., 2017; Guzavina et al., 2019; Zhang et al., 2023). The second approach, known as local or regional induction studies, involves observing a relatively small area of the Earth's surface, which is typically assumed to be flat. The MT method falls under this category.

Srivastava (1966) and Utada (2018) demonstrated that, when the induction wavenumber dominates the source wavenumber, MT impedances in both spherical and flat Earth models are equivalent, provided the Earth's structure is one-dimensional (1-D). However, MT studies are generally conducted under the flat Earth approximation, even when the three-dimensional (3-D) structure of the Earth is considered. This approximation is deemed valid for regional- and local-scale approaches conducted at mid-low latitudes and for periods up to a few hours (e.g., Simpson & Bahr, 2005; Chave & Jones, 2012). As a result, modeling in a Cartesian coordinate system is typically preferred in MT studies due to its simplicity and advanced development compared to spherical coordinate system modeling. Advances in computational power have further facilitated the progress in 3-D MT modeling and inversion techniques. These developments now allow MT surveys to be conducted at hundreds of sites, enabling extensive spatial coverage suitable for investigating the Earth's 3-D structure (e.g., Wannamaker et al., 1984; Mackie et al., 1993, 1994; Newman & Alumbaugh, 2000; Siripunvaraporn et al., 2005; Egbert & Kelbert, 2012).

However, 3-D modeling in a Cartesian coordinate system requires additional considerations. A Cartesian model serves as a substitute for a spherical model to study 3-D Earth structures, ignoring the Earth's curvature. This approach necessitates the use of map projections, which inevitably result in geometric distortions (Utada 2018; Grayver et al., 2019) because no map projection can simultaneously preserve area, distance, and angle. In certain cases, the modeling domain of a regional study extends horizontally over several thousand to ten thousand kilometers to account for the influence of distant lateral conductivity contrasts, such as those due to coastlines (e.g., Baba et al., 2010). Under such conditions, 3-D MT inversion using a forward code in a Cartesian coordinate system may produce artifacts due to geometric distortions introduced by a map projection. Several recent studies have identified this issue and attempted to perform 3-D MT modeling of a laterally heterogeneous Earth using spherical models to quantitatively assess the validity of employing Cartesian models for regional MT studies (Grayver et al., 2019; Luo et al., 2019; Han et al., 2020; Han & Hu, 2023). These investigations evaluated the differences between impedances calculated in Cartesian and spherical coordinate systems. However, differences exist among these studies, including the treatment of conductivity models and the source.

Regarding the treatment of the models, Grayver et al. (2019), Han et al. (2020), and Han and Hu (2023) examined the impedance of continental (land) regions to evaluate their modeling results. However, considering the presence of highly conductive seawater with complex bathymetric undulations and coastlines, a stronger lateral heterogeneity effect on EM induction is expected in oceanic regions. In this study, we first focus on modeling MT impedances in an oceanic region of the Philippine Sea, where a three-year-long seafloor EM survey was conducted (e.g., Baba et al., 2010; Tada et al., 2014). For comparison, we also examine the behaviors of MT impedances in a continental region of the Qinghai-Tibet Plateau in southwestern China, where a large-scale MT array study was conducted (e.g., Yang et al., 2020).

Regarding the treatment of the source, Luo et al. (2019), Han et al. (2020), and Han and Hu (2023) applied a combination of two orthogonal external magnetic dipoles. These dipoles generate spatially uniform fields to represent the external magnetic fields that are tangential and oriented northward and eastward, respectively, at the intersection of the equator and central meridian. Grayver et al. (2019) applied another source combination comprising three orthogonal external magnetic dipoles to ensure the matrix for calculating impedances anywhere on the Earth remains of full rank. In their study, two of the three dipoles matched those used by Luo et al. (2019), Han et al. (2020), and Han and Hu (2023), while the third dipole represented the external magnetic field directed radially at the intersection.

In a Cartesian model under the plane wave approximation, any pair of linearly independent sources provide unique values of impedance elements, regardless of their amplitude and polarization (Berdichevsky and Dmitriev, 1997; Berdichevsky, 1999). Therefore, in a Cartesian coordinate system, the source effect refers to the source wavenumber effect (also known as the source dimension effect; see Appendix A), which has been the focus of most related studies in the past (e.g., Schmucker, 1987; Garcia et al., 1997). However, few studies have explored source effects on MT impedances in a spherical coordinate system. This gap in literature has motivated the present study.

When the plane-wave approximation is not considered, there are three kinds of source effect in MT: harmonic degree (wave number), polarization, and amplitude effects. Although previous studies employing spherical models have applied different source combinations, none have systematically examined the source effect on the MT impedance (Grayver et al., 2019; Luo et al., 2019; Han et al., 2020; Han & Hu, 2023). This represents a critical issue, as the MT impedance under plane-wave approximation intended to function as a response dependent solely on frequency and subsurface electrical conductivity distribution, and not on the source. In this study, we focus on the presence or absence of a source amplitude effect in spherical impedance estimates. More specifically, we address whether the impedances obtained from various source combinations in a spherical model are consistent, particularly with respect to the amplitude of each external dipole source.

2 Formulations

2.1 Basic equations and coordinate systems

In this study, we perform MT forward modeling in a spherical coordinate system. We solve the basic equations for the time-varying EM field (Maxwell's equations) in the frequency domain as follows:

$$\nabla \times \mathbf{E}(\mathbf{r}, \omega) = -i\omega\mu\mathbf{H}(\mathbf{r}, \omega), \tag{1}$$

$$\nabla \times \mathbf{H}(\mathbf{r}, \omega) = \sigma(\mathbf{r})\mathbf{E}(\mathbf{r}, \omega) + \mathbf{j}^{ext}(\mathbf{r}, \omega), \tag{2}$$

where $\mathbf{E}(\mathbf{r}, \omega)$ and $\mathbf{H}(\mathbf{r}, \omega)$ denote the electric and magnetic fields at position $\mathbf{r}$ and angular frequency ω. Here, i denotes the imaginary unit, μ the magnetic permeability, $\sigma(\mathbf{r})$ the electrical conductivity, and $\mathbf{j}^{ext}(\mathbf{r}, \omega)$ the source electric current density. The displacement current is ignored in Eq. (2). We assume $\mu = \mu_0$ everywhere, where μ_0 represents the magnetic permeability of vacuum. We consider periods between 1,000 and 10,000 sec in modeling an oceanic region and between 100 and 10,000 sec in modeling a continental region.

The position vector at any location in a geographic spherical coordinate system, with respect to the reference coordinate system (ξ, η, ζ), is defined as $\mathbf{r} = (r, \theta, \varphi)^t$, where the center of the Earth is taken as the origin (Figure 1a). Here, r, θ, and φ denote the distance from the origin, colatitude, and longitude, respectively. Superscript t indicates the transpose.

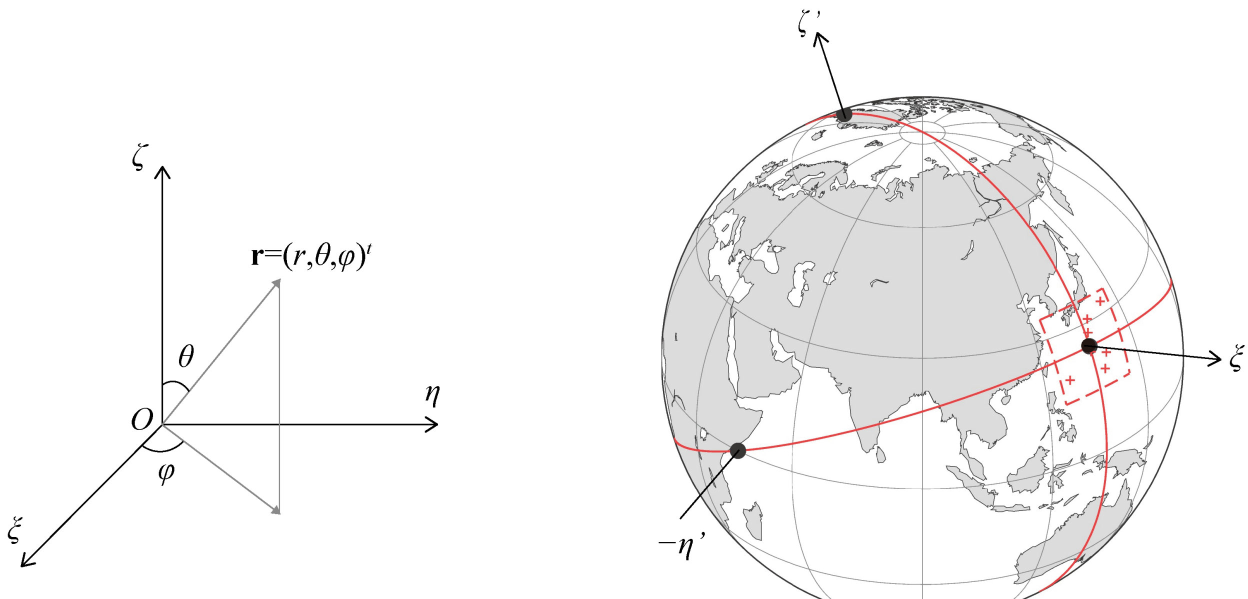

(a) (b)

Figure 1. (a) A spherical coordinate system with the center of the Earth as the origin. (b) Coastlines on the spherical Earth. The two great circles shown as red lines represent the equator and central meridian in the rotated spherical coordinate system. Black dots mark the positions where the ξ', η' or ζ'- axis intersects the Earth's surface. The area enclosed by the red dashed lines indicates the study region for the oceanic model. Red crosses denote locations of the seven selected sites considered in later sections.

For numerical modeling, the longitudinal grids may become asymmetric between the northern and southern parts of the study region if the center of the study region is not located at the equator. Such asymmetry can lead to differences in computational precision between the northern and southern parts of the study region (a portion of the spherical surface). To mitigate this effect, we introduce a rotation of the reference coordinate system from (ξ, η, ζ) to (ξ', η', ζ') using two of the three Euler angles, α and β (See Figure S1). The position vector with respect to the rotated reference coordinate system (ξ', η', ζ') is denoted as $\mathbf{r}' = (r, \theta', \varphi')^t$. In this study, we rotate the reference coordinate system to align the intersection of the equator and central meridian in the rotated system ($\theta' = 90°$ and $\varphi' = 0°$) with the center of the study region as shown in Figure 1b.

It is important to note that the introduction of coordinate rotation in our study is not only aimed at improving computational precision within a fixed coordinate system but also at enabling a rigorous comparison between results obtained in Cartesian and spherical coordinates at the same location with the same structural model. Moreover, when performing electromagnetic modeling and inversion in spherical coordinates for real data applications, achieving the highest possible computational accuracy becomes essential. Therefore, incorporating coordinate rotation enhances both the accuracy of our current study and its applicability to future research.

2.2 MT impedance and deviation

Using the solutions of the basic equations, we can calculate the MT impedance $\mathbf{Z}$, which relates the electric and magnetic fields as follows:

$$\mathbf{E}(\mathbf{r}_{ob},\omega) = \mathbf{Z}(\mathbf{r}_{ob},\omega)\mathbf{H}(\mathbf{r}_{ob},\omega) + \delta\boldsymbol{\epsilon}_{\mathbf{E}} \tag{3}$$

at an arbitrary observation site $\mathbf{r}_{ob}$ and angular frequency ω. $\delta\boldsymbol{\epsilon}_{\mathbf{E}}$ is the residual term and the impedance is determined by solving a least squares problem to minimize $\delta{\boldsymbol{\epsilon}_{\mathbf{E}}}^2$. In conventional MT, two horizontal components of the EM fields are considered in Eq. (3); therefore, the impedance is a complex-valued 2 × 2 (4-element) tensor.

In this study, the location of each observation site is specified by the colatitude (θ) and longitude (φ) in the original spherical coordinate system. At any observation site, the directions of tangential axes in the rotated spherical coordinate system (positive θ' and φ') deviate from those of positive θ and φ in the original spherical coordinate system. The impedance elements calculated by modeling in the rotated spherical coordinate system were converted to those defined in the original spherical coordinate system to ensure consistency with actual field measurements. The four impedance elements are denoted as $Z_{ij}(\mathbf{r}_{ob},\omega)$ where subscripts i and j denote θ or φ. Hereafter, the position and frequency dependences of electromagnetic fields and impedances, $(\mathbf{r}_{ob},\omega)$, are omitted for simplicity.

To compare the impedances calculated at a location $\mathbf{r}_{ob}$ and frequency ω under different conditions (source combinations, for example) 1 and 2, we use the Frobenius norm (F-norm) deviation, defined as:

$$dZ^{1-2} = \frac{\|\mathbf{Z}^1 - \mathbf{Z}^2\|_F}{\|\mathbf{Z}^2\|_F}, \tag{4}$$

where $\mathbf{Z}^1$ and $\mathbf{Z}^2$ are the two impedances to be compared. The F-norm of $\mathbf{Z}$ is defined as:

$$\|\mathbf{Z}\|_F = \{\mathrm{tr}(\mathbf{Z}^H\mathbf{Z})\}^{1/2} = \left\{\sum_{i,j}\left|Z_{ij}\right|^2\right\}^{1/2}, \tag{5}$$

where superscript H denotes the Hermitian (complex conjugate) transpose.

In certain cases, we calculate the average F-norm deviation over the entire study region, which is defined as:

$$dZ_{avg}^{1-2} = \frac{1}{N}\sum_{n=1}^{N}\frac{\|\mathbf{Z}_n^1 - \mathbf{Z}_n^2\|_F}{\|\mathbf{Z}_n^2\|_F}, \tag{6}$$

where subscript n represents a calculation cell, and N is the total number of calculation cells in the study region on the seafloor (oceanic model) or the surface (continental model).

In this study, we set the target level of the F-norm deviation of impedance to 0.01, which is a typical error level of the MT impedance in case of seafloor observations (Tada et al., 2012). In subsequent comparisons, two impedances are considered consistent when the F-norm deviation is smaller than this target level.

To represent the complex-valued elements of the impedance, the apparent resistivity and impedance phase are also used, defined as:

$$\rho_{a_{ij}} = \frac{|Z_{ij}|^2}{\omega\mu_0} \tag{7}$$

and

$$\phi_{ij} = \arg[Z_{ij}], \tag{8}$$

respectively. In several cases, we compared the spatial distributions and differences of the numerically calculated ρ_{aij} and ϕ_{ij}, along with the F-norm deviation of the impedance Z, between two modeling results. The differences in ρ_{aij} and ϕ_{ij} are defined as:

$$d\rho_{a_{ij}}^{1-2} = \frac{\rho_{a_{ij}}^{1}}{\rho_{a_{ij}}^{2}} \tag{9}$$

and

$$d\phi_{ij}^{1-2} = \phi_{ij}^1 - \phi_{ij}^2, \tag{10}$$

respectively.

2.3 External source

In a rotated spherical coordinate system, we consider an external magnetic source of spherical harmonic degree one (dipole term), which generates a spatially uniform field. The external magnetic field above the Earth's surface ($r > r_e$, where $r_e = 6371$ km is the Earth's radius) can be obtained from the spatial gradient of the scalar potential, generally expressed by the spherical harmonic expansion as:

$$V(r,\theta',\varphi',\omega) = r(q_1^0(\omega)\cos\theta' + q_1^1(\omega)\cos\varphi'\sin\theta' + s_1^1(\omega)\sin\varphi'\sin\theta'), \tag{11}$$

where $q_1^0(\omega)$, $q_1^1(\omega)$, and $s_1^1(\omega)$ are expansion coefficients of the axial and two equatorial dipole terms, respectively.

Using $\mathbf{B} = -\nabla V$ and $\mathbf{H} = \frac{\mathbf{B}}{\mu_0}$, the three components of the external magnetic field are obtained as:

$$H_r(r,\theta',\varphi',\omega) = -\frac{1}{\mu_0}(q_1^0(\omega)\cos\theta' + q_1^1(\omega)\cos\varphi'\sin\theta' + s_1^1(\omega)\sin\varphi'\sin\theta'), \tag{12}$$

$$H_\theta(r,\theta',\varphi',\omega) = -\frac{1}{\mu_0}(-q_1^0(\omega)\sin\theta' + q_1^1(\omega)\cos\varphi'\cos\theta' + s_1^1(\omega)\sin\varphi'\cos\theta'), \tag{13}$$

and

$$H_\varphi(r,\theta',\varphi',\omega) = -\frac{1}{\mu_0}(-q_1^1(\omega)\sin\varphi' + s_1^1(\omega)\cos\varphi'). \tag{14}$$

For convenience, we represent the three basis sources (external dipoles) in the rotated spherical coordinate system by three unit vectors in ζ', ξ', and η' directions, denoted as $\hat{\mathbf{S}}_{\zeta'}$, $\hat{\mathbf{S}}_{\xi'}$, and $\hat{\mathbf{S}}_{\eta'}$, corresponding to the harmonic expansion coefficients q_1^0, q_1^1, and s_1^1, respectively (Figure 2a).

By setting $\frac{q_1^0(\omega)}{\mu_0} = \frac{q_1^1(\omega)}{\mu_0} = \frac{s_1^1(\omega)}{\mu_0} = -1$, these sources generate uniform magnetic fields of unit amplitude in the positive ζ'-, ξ'-, and η'- directions, respectively. An arbitrary source in the rotated spherical coordinate system, denoted as $\mathbf{S}(\theta_S', \varphi_S')$ is specified by the pole location (θ_S', φ_S') (Figure 2b). The source $\mathbf{S}$ can be expressed by a linear combination of the three basis sources:

$$\mathbf{S}(\theta_S', \varphi_S') = a_{\zeta'}\hat{\mathbf{S}}_{\zeta'} + a_{\eta'}\hat{\mathbf{S}}_{\eta'} + a_{\xi'}\hat{\mathbf{S}}_{\xi'}, \tag{15}$$

where $a_{\zeta'}$, $a_{\eta'}$, and $a_{\xi'}$ are real-valued arbitrary amplitude factors. For a normalized source, the unit amplitude expression in an arbitrary direction is given by:

$$\hat{\mathbf{S}}(\theta_S', \varphi_S') = \hat{a}_{\zeta'}\hat{\mathbf{S}}_{\zeta'} + \hat{a}_{\eta'}\hat{\mathbf{S}}_{\eta'} + \hat{a}_{\xi'}\hat{\mathbf{S}}_{\xi'}, \tag{16}$$

where

$$\hat{a}_{\zeta'} = \frac{a_{\zeta'}}{|\mathbf{S}(\theta_S', \varphi_S')|} = \cos\theta_S', \tag{17}$$

$$\hat{a}_{\eta'} = \frac{a_{\eta'}}{|\mathbf{S}(\theta_S', \varphi_S')|} = \sin\theta_S' \sin\varphi_S', \tag{18}$$

and

$$\hat{a}_{\xi'} = \frac{a_{\xi'}}{|\mathbf{S}(\theta_S', \varphi_S')|} = \sin\theta_S' \cos\varphi_S'. \tag{19}$$

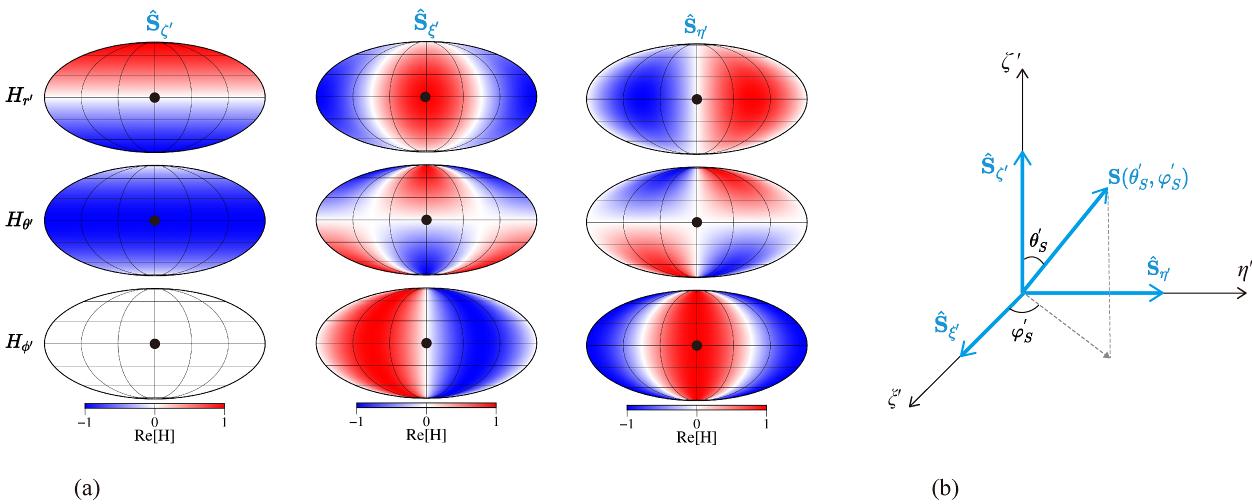

Figure 2. (a) Distribution of magnetic field components on a spherical surface for the three basis sources in the rotated coordinate system. The black dots mark the location of the intersection of the equator and central meridian. (b) External dipole sources in the rotated coordinate system. $\mathbf{S}$ is a source dipole of arbitrary polarization and amplitude with one of its poles located at (θ_S', φ_S').

The external field generated by an arbitrary source $\mathbf{S}$ is expressed as $\mathbf{H}_{ext}(r, \theta', \varphi', \omega, \mathbf{S})$. Using Eq. (15) and the linearity of the EM field, this can be written as:

$$\mathbf{H}_{ext}(r, \theta', \varphi', \omega, \mathbf{S}) = a_{\zeta'}\mathbf{H}_{ext}(r, \theta', \varphi', \omega, \hat{\mathbf{S}}_{\zeta'}) + a_{\eta'}\mathbf{H}_{ext}(r, \theta', \varphi', \omega, \hat{\mathbf{S}}_{\eta'}) + a_{\xi'}\mathbf{H}_{ext}(r, \theta', \varphi', \omega, \hat{\mathbf{S}}_{\xi'}), \tag{20}$$

where

$$\mathbf{H}_{ext}\left(r,\theta',\varphi',\omega,\hat{\mathbf{S}}_{\zeta'}\right) = -\frac{q_1^0(\omega)}{\mu_0}\begin{pmatrix}\cos\theta' \\ -\sin\theta' \\ 0\end{pmatrix} = \begin{pmatrix}\cos\theta' \\ -\sin\theta' \\ 0\end{pmatrix}, \tag{21}$$

$$\mathbf{H}_{ext}\left(r,\theta',\varphi',\omega,\hat{\mathbf{S}}_{\eta'}\right) = -\frac{q_1^1(\omega)}{\mu_0}\begin{pmatrix}\sin\theta'\cos\varphi' \\ \cos\theta'\cos\varphi' \\ -\sin\varphi'\end{pmatrix} = \begin{pmatrix}\sin\theta'\cos\varphi' \\ \cos\theta'\cos\varphi' \\ -\sin\varphi'\end{pmatrix}, \tag{22}$$

and

$$\mathbf{H}_{ext}\left(r,\theta',\varphi',\omega,\hat{\mathbf{S}}_{\xi'}\right) = -\frac{s_1^1(\omega)}{\mu_0}\begin{pmatrix}\sin\theta'\sin\varphi' \\ \cos\theta'\sin\varphi' \\ \cos\varphi'\end{pmatrix} = \begin{pmatrix}\sin\theta'\sin\varphi' \\ \cos\theta'\sin\varphi' \\ \cos\varphi'\end{pmatrix}. \tag{23}$$

These external fields given in Eq. (21)-(23) correspond to $-H^1$, $-H^2$, and $-H^3$ in Grayver et al. (2019).

The Maxwell's equations are solved by providing a source boundary condition at the outer boundary of the model domain using Eqs. (21)–(23). The resulting solutions for the source $\hat{\mathbf{S}}_{\zeta'}$, for example, are denoted as $\mathbf{E}\left(r,\theta',\varphi',\omega,\hat{\mathbf{S}}_{\zeta'}\right)$ and $\mathbf{H}\left(r,\theta',\varphi',\omega,\hat{\mathbf{S}}_{\zeta'}\right)$. The solutions for an arbitrary source $\mathbf{S}$ can then be obtained as a linear combination of the solutions for the three basis sources:

$$\mathbf{E}(r,\theta',\varphi',\omega,\mathbf{S}) = a_{\zeta'}\mathbf{E}\left(r,\theta',\varphi',\omega,\hat{\mathbf{S}}_{\zeta'}\right) + a_{\eta'}\mathbf{E}\left(r,\theta',\varphi',\omega,\hat{\mathbf{S}}_{\eta'}\right) + a_{\xi'}\mathbf{E}\left(r,\theta',\varphi',\omega,\hat{\mathbf{S}}_{\xi'}\right) \tag{24}$$

and

$$\mathbf{H}(r,\theta',\varphi',\omega,\mathbf{S}) = a_{\zeta'}\mathbf{H}\left(r,\theta',\varphi',\omega,\hat{\mathbf{S}}_{\zeta'}\right) + a_{\eta'}\mathbf{H}\left(r,\theta',\varphi',\omega,\hat{\mathbf{S}}_{\eta'}\right) + a_{\xi'}\mathbf{H}\left(r,\theta',\varphi',\omega,\hat{\mathbf{S}}_{\xi'}\right), \tag{25}$$

respectively.

In this numerical modeling study, the MT impedance is estimated from the EM field solutions by providing a set of external dipole sources. A set of two or three sources is denoted by $\{\mathbf{S}_1, \mathbf{S}_2\}$ or $\{\mathbf{S}_1, \mathbf{S}_2, \mathbf{S}_3\}$, respectively, where $\mathbf{S}_1$, $\mathbf{S}_2$, and $\mathbf{S}_3$ are external dipole sources with arbitrary directions and amplitudes.

3 Model setup

3.1 Modeling methods and surface inhomogeneities

Modeling in a spherical coordinate system was performed using a global forward code modified from Uyeshima and Schultz (2000). This code employs a staggered-grid finite difference method to solve Maxwell's equations, with all variables calculated in double precision. The source field, as expressed in Eq. (20), was set at the outer boundary of the model domain ($r = 10r_e$). The source altitude was chosen sufficiently far from the Earth's surface to ensure that the internal part of the primary field is negligible. The inner boundary was set at the core-mantle boundary (CMB) ($r = 3479$ km), where the radial magnetic field component is set to zero as a boundary condition. Convergence of the numerical solution was confirmed through iteration, when the normalized change in the magnetic field solution, defined by the dot products of the magnetic vector integrated over the entire calculation domain, reached 10^{-16}.

The model assumes the Earth's interior to consists of two thin, laterally heterogeneous shells on the surface and a 1-D (radially symmetric) structure beneath them. The shallowest layer is a 4-km-thick inhomogeneous shell representing the land-sea electrical conductivity contrast, with variable conductance reflecting bathymetric undulations. Land topography is ignored because conductance is smaller on land than in the sea. The second layer is a 1-km-thick inhomogeneous shell that simulating lateral variations in oceanic sediment thickness. Figure 3 shows the assumed 1-D profile below these two shells, which was designed with reference to the oceanic mantle model of the western Pacific (Baba et al., 2010; Shimizu et al., 2010), with simplifications.

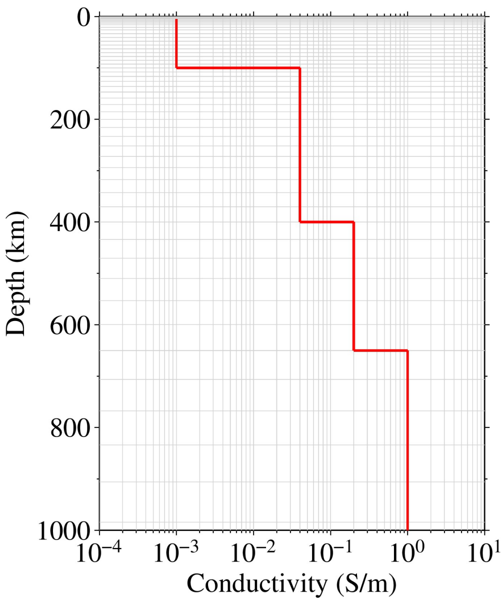

Figure 3. 1-D electrical conductivity structure and the radial gridding (depth from 5 km to 1,000 km) assumed for the numerical models. The structure is designed by considering the 1-D structures beneath the Pacific obtained by Baba et al. (2010) and Shimizu et al. (2010).

We assumed electrical conductivities of the sea water, sediment, and crustal rock in the two surface shells to be 3.0, 0.1, and 0.01 S/m, respectively. For the oceanic area of the surface shell, we first averaged the bathymetry data from ETOPO1 (Amante & Eakins, 2009), which originally had a resolution of $1' \times 1'$, within each cell. The conductance and average conductivity in the 4 km-thick surface shell were calculated under the assumption of homogeneous conductivity within each cell. For the sediment shell, we employed the Laske and Masters (1997) model. The sediment thickness, originally provided at a resolution of $1° \times 1°$, was first interpolated, and then the conductance and average conductivity were calculated in a manner similar to that used for the first shell. In the oceanic model, the MT impedance was estimated at the seafloor (the boundary between the top two heterogeneous shells) using the modeled EM solutions. In the continental model, the MT impedance was estimated at the surface.

3.2 Grid spacing

We adopted identical grid spacings for both the oceanic and continental models to facilitate comparison. Because it is not practical to solve the basic equations with a fine grid spacing across the entire modeling domain, non-uniform gridding is applied in both the radial and tangential directions. The lateral size of the study region was defined as $20° \times 20°$. The center of the study region was set at (25°N, 135°E) for the oceanic model and at (32°N, 90° E) for the continental model. These center locations were then positioned at (0°N, 0°E) in the rotated coordinate system.

The radial grid spacing was uniformly set to 500 m in the land-sea contrast shell and to 250 m in the sediment shell. In the 1-D shells, the radial grid spacing gradually increased following logarithmic equidistance (Fujita et al., 2018) until the CMB. The lateral grid size was set to 0.25° in the central area, including the study region, and gradually widened to 1°, 2°, and 5°, depending on the distance from the center. The area of the finest (0.25°) grids was defined as 40° × 40° based on numerical tests (Figure 4, S2, and Table S1 for the influence of the area of the finest grids). The radial grid spacing near the seafloor was confirmed to be sufficiently fine for the 3-D model (Figure S3). In total, the grid system consisted of 89 cells in the r-direction, including 17 cells in the air, 194 cells in the θ'-direction, and 230 cells in the φ'-direction.

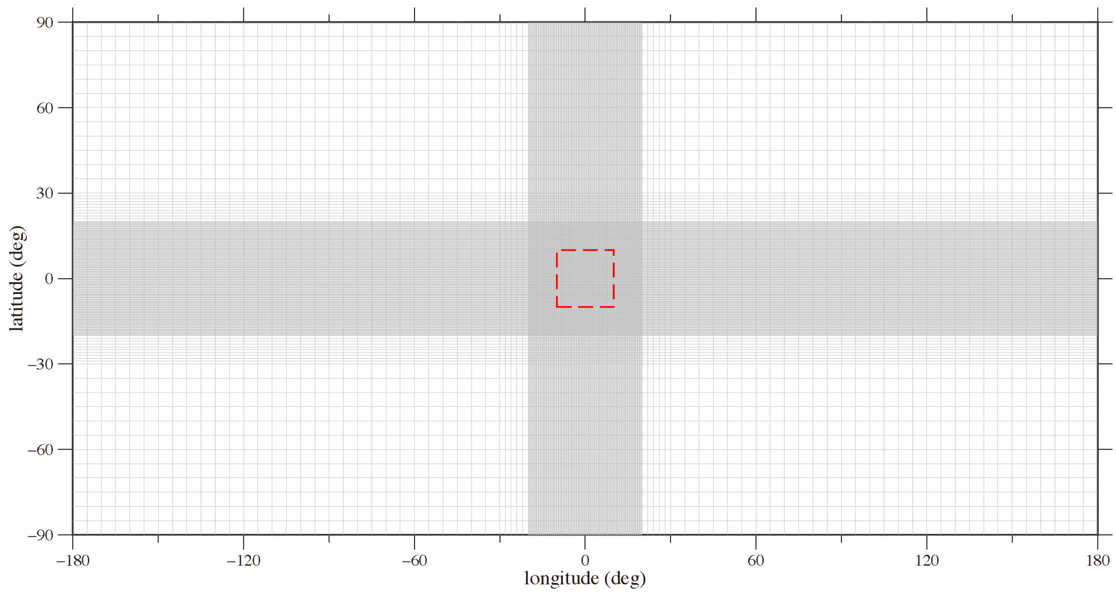

Figure 4. Lateral grid spacing for spherical model in the rotated coordinate system. The red dashed square indicates the study region.

4 Influence of the source on estimating the MT impedance in a spherical model

To obtain four elements of the MT impedance from the EM components of numerical modeling solutions, at least two linearly independent sources are required. In the case of a Cartesian model under the plane-wave approximation, the MT impedance is known to be independent of the source amplitude and polarization, and therefore serves as an EM response function of the Earth (See Appendix B). In a spherical model, the conventional impedance, consisting of four elements, can be estimated from the EM solutions for two independent sources by solving (Grayver et al., 2019)

$$\begin{pmatrix} E_\theta^1 & E_\theta^2 \\ E_\varphi^1 & E_\varphi^2 \end{pmatrix} = \begin{pmatrix} Z_{\theta\theta} & Z_{\theta\varphi} \\ Z_{\varphi\theta} & Z_{\varphi\varphi} \end{pmatrix} \begin{pmatrix} H_\theta^1 & H_\theta^2 \\ H_\varphi^1 & H_\varphi^2 \end{pmatrix}, \tag{26}$$

where superscripts 1 and 2 denote two linearly independent external sources.

By re-writing Eq. (26), we obtain a positive definite system of equations $\boldsymbol{b} = \boldsymbol{Ax}$, where $\boldsymbol{b}$ is a vector composed of modelled electric field components E_θ^1, E_θ^2, E_φ^1, and E_φ^2, $\boldsymbol{A}$ is a matrix composed of modelled magnetic components H_θ^1, H_θ^2, H_φ^1, and H_φ^2, and $\boldsymbol{x}$ is a vector composed of four impedance elements $Z_{\theta\theta}, Z_{\theta\varphi}$, $Z_{\varphi\theta}$, and $Z_{\varphi\varphi}$. The unknown vector $\boldsymbol{x}$ can be obtained by

$$\boldsymbol{x} = (\boldsymbol{A}^H \boldsymbol{A})^{-1} \boldsymbol{A}^H \boldsymbol{b}. \tag{27}$$

Grayver et al. (2019) pointed out that solving Eq. (27) is not globally feasible because matrix A may not be of full rank at the pole location of the source dipole field. However, it is possible to estimate four elements of the impedance using two independent sources within a specific part of the Earth's surface (the study region), where the matrix rank is confirmed to be full.

Here, we considered the oceanic model (Figure 5a), which includes the study region of a seafloor MT experiment conducted in the Philippine Sea by Baba et al. (2010). We calculated the MT impedances in the rotated spherical coordinate system for two periods: 1,000 and 10,000 sec. We compared two results obtained by using different combinations of external dipole sources of unit intensity: $\{\hat{\mathbf{S}}_{\zeta'}, \hat{\mathbf{S}}_{\eta'}\}$ and $\{\hat{\mathbf{S}}(45°, 45°), \hat{\mathbf{S}}(135°, 45°)\}$. The first source combination provides the best similarity to MT modeling in a Cartesian coordinate system with two orthogonal plane-wave sources polarized in the N-S and E-W directions. These two combinations are chosen for this experiment because they exhibit the largest angular distance from each other. The results at seven selected sites showed significant F-norm deviations (Figure 5b), indicating that the impedance estimated using these two sources is non-unique but depends on the source polarization. Through further systematic numerical experiments, we confirmed that in a spherical coordinate system, impedances obtained from an arbitrary pair of orthogonal sources are unique only when the sources lie within a single great circle plane and have no components normal to that plane.

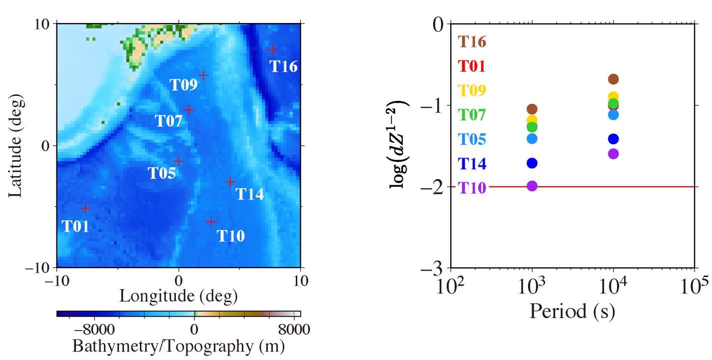

(a) (b)

Figure 5. (a) A map showing the bathymetry and site locations of the oceanic model. Red crosses show the seven selected sites (after Baba et al., 2010). (b) F-norm deviations at seven selected sites between calculated impedances with source combinations of $\{\hat{\mathbf{S}}(45°, 45°), \hat{\mathbf{S}}(135°, 45°)\}$ and $\{\hat{\mathbf{S}}_{\zeta'}, \hat{\mathbf{S}}_{\eta'}\}$. Model: the oceanic model in a rotated spherical coordinate system.

Next, we consider three independent sources to estimate the impedance, as suggested by Grayver et al. (2019), to address the problem of non-uniqueness in impedance determination. We attempted to estimate the four elements of the MT impedance from the modeling results with three orthogonal sources of unit amplitude by solving the matrix equation of an overdetermined system:

$$\begin{pmatrix} E_\theta^1 & E_\theta^2 & E_\theta^3 \\ E_\varphi^1 & E_\varphi^2 & E_\varphi^3 \end{pmatrix} = \begin{pmatrix} Z_{\theta\theta} & Z_{\theta\varphi} \\ Z_{\varphi\theta} & Z_{\varphi\varphi} \end{pmatrix} \begin{pmatrix} H_\theta^1 & H_\theta^2 & H_\theta^3 \\ H_\varphi^1 & H_\varphi^2 & H_\varphi^3 \end{pmatrix} + \begin{pmatrix} \delta\epsilon_{E_\theta}^1 & \delta\epsilon_{E_\theta}^2 & \delta\epsilon_{E_\theta}^3 \\ \delta\epsilon_{E_\varphi}^1 & \delta\epsilon_{E_\varphi}^2 & \delta\epsilon_{E_\varphi}^3 \end{pmatrix}, \tag{28}$$

where superscripts 1, 2, and 3 represent the EM solutions for the respective independent sources. Rewriting Eq. (28), we obtain an overdetermined system of linear equations $\boldsymbol{b} = \boldsymbol{Ax} + \delta\boldsymbol{\epsilon}_{\mathbf{E}}$, which can be solved by minimizing the residual term, as in the case of Eq. (27).

Similar to the previous experiment, the modelled impedances were examined and compared using two different source combinations in the oceanic model. In each source combination, two sources were kept to be the same as in the previous case, and a third source orthogonal to the other two was added. The source combinations considered are $\{\hat{\mathbf{S}}_{\zeta'}, \hat{\mathbf{S}}_{\eta'}, \hat{\mathbf{S}}_{\xi'}\}$ and $\{\hat{\mathbf{S}}(45°, 45°), \hat{\mathbf{S}}(135°, 45°), \hat{\mathbf{S}}(90°, 135°)\}$. The newly added basis source, $\hat{\mathbf{S}}_{\xi'}$, produces a magnetic field only in the radial direction at the center of the study region in the rotated spherical coordinate system.

For both source combinations, the four elements of the MT impedance were estimated using Eq. (28). The F-norm deviations at all selected sites turned out very small, at the level of 10^{-9}, indicating that the impedances estimated from the two source combinations were consistent. Differences in the apparent resistivities and impedance phases were also sufficiently small, at a level of 10^{-9}–10^{-8} (See Figure S5).

The source combinations described above, which provide unique impedances, consist of three mutually orthogonal external dipole sources with equal (unit) amplitudes. However, natural source fields (geomagnetic disturbances) are complex; their amplitudes and polarizations change dynamically over time. To examine whether more complex source combinations with different polarizations and amplitudes yield unique impedances as shown above, we conducted further numerical experiments and compared the impedances estimated from various source combinations. When one of the three sources is not orthogonal to the other two, it can be decomposed into three sources so that one of them is orthogonal to the other two, thereby independently contributing to impedance estimation. Thus, the source polarization effect can essentially be regarded as a source amplitude effect. We considered cases in which two of the three orthogonal sources had unit amplitudes, while the amplitude of the third source was varied.

The source combinations examined were: $\{a_1\hat{\mathbf{S}}(45°, 45°), \hat{\mathbf{S}}(135°, 45°), \hat{\mathbf{S}}(90°, 135°)\}$, $\{\hat{\mathbf{S}}(45°, 45°), a_2\hat{\mathbf{S}}(135°, 45°), \hat{\mathbf{S}}(90°, 135°)\}$ and $\{\hat{\mathbf{S}}(45°, 45°), \hat{\mathbf{S}}(135°, 45°), a_3\hat{\mathbf{S}}(90°, 135°)\}$ where amplitude factor, a_1, a_2, and a_3 took values $10^{-0.5}$, 1, and $10^{0.5}$, respectively. The impedances calculated from these source combinations in the oceanic model were compared with those obtained from the reference source combination $\{\hat{\mathbf{S}}_{\zeta'}, \hat{\mathbf{S}}_{\eta'}, \hat{\mathbf{S}}_{\xi'}\}$. The F-norm deviations of the impedance obtained at seven selected sites exceeded 0.01 at most sites when a_1, a_2, or a_3 was $10^{-0.5}$ or $10^{0.5}$ (See Figure S6). Additionally, the largest deviation occurred at T16 or T09, while the smallest deviation was observed at T10, suggesting that the deviation decreases with increasing distance from the coastlines and/or the areas with steep bathymetric changes. Differences in the apparent resistivity and impedance phase also showed significant anomalies not only near coastlines but also in flat basins (see Figure S7 for the case where a_1 is $10^{-0.5}$). These results suggest that the impedance estimated from the three independent sources depends on the source amplitude.

Next, the average F-norm deviation of the impedance was calculated for the entire study region over a wider range of amplitude factors. The impedances obtained from different values of a_1, a_2, and a_3 were compared with those from the reference source combination consisting of three basis sources. The amplitude factors a_1 (represented by open blue circles), a_2 (represented by solid blue squares), and a_3 (represented by open blue squares) varied between 10^{-5} and 10^5. The results are shown in Figure 6. We found that the averaged deviations were approximately 10^{-9} only when a_1, a_2, and a_3 were exactly 1. Outside this narrow range near unity, the F-norm deviations exceeded the typical observation error level (0.01), with the largest deviation at a level of 0.1. The deviations also exhibited slight asymmetry with respect to the unit amplitudes. The results of these numerical experiments clearly indicate that the MT impedance consisting of four elements is not unique and depends on the source amplitude.

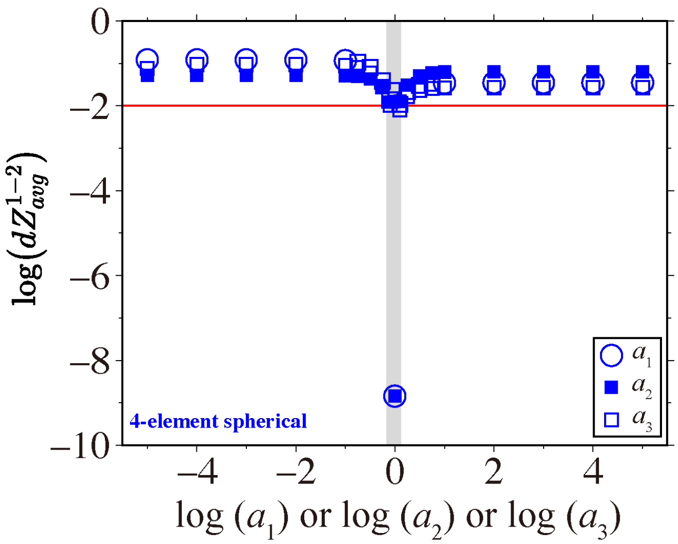

Figure 6. Dependence of dZ_{avg}^{1-2} on $\log(a_1)$, $\log(a_2)$, or $\log(a_3)$ in a range when a_1, a_2 or a_3 is between 10^{-5} and 10^5 in the entire study region at period of 10,000 sec. Open blue circles represent $d\mathbf{Z}_{avg}^{1-2}$ between the 4-element impedances from source combination of $\{a_1\hat{\mathbf{S}}(45°, 45°),$ $\hat{\mathbf{S}}(135°, 45°), \hat{\mathbf{S}}(90°, 135°)\}$ and from $\{\hat{\mathbf{S}}_{\zeta'}, \hat{\mathbf{S}}_{\eta'}, \hat{\mathbf{S}}_{\xi'}\}$, solid blue squares between those from source combination of $\{\hat{\mathbf{S}}(45°, 45°), a_2\hat{\mathbf{S}}(135°, 45°), \hat{\mathbf{S}}(90°, 135°)\}$ and from $\{\hat{\mathbf{S}}_{\zeta'}, \hat{\mathbf{S}}_{\eta'}, \hat{\mathbf{S}}_{\xi'}\}$, and open blue squares between those from $\{\hat{\mathbf{S}}(45°, 45°), \hat{\mathbf{S}}(135°, 45°), a_3\hat{\mathbf{S}}(90°, 135°)\}$, and $\{\hat{\mathbf{S}}_{\zeta'}, \hat{\mathbf{S}}_{\eta'}, \hat{\mathbf{S}}_{\xi'}\}$. Hatched area corresponds to horizontal range of a_i considered in Section 6. Model: the oceanic model in a rotated spherical coordinate system.

We conducted an additional experiment on the continental model of the Qinghai-Tibet Plateau region (Figure 7a). Two tests were performed: one with and one without a highly conductive anomaly (Yang et al., 2020). In the model with the anomaly, a polygonal structure with a conductivity of 0.1 S/m was assumed, centered in the study region and to have dimensions of 16° × 6° laterally (represented by the green rectangle in Figure 7a), extending from 4 to 100 km in depth. In the absence of the 3-D anomaly, the model is nearly 1-D because the study region is far from the coastlines and the crust and mantle are assumed to be laterally homogeneous with a conductivity of 100 S/m.

We first examined the case without a 3-D anomaly and estimated the four elements of the impedance at five selected sites, L05, L02, L03, L01, and L04 (Yang et al., 2020, see Figure 7a for their locations), where MT measurements were conducted. The estimations were made for three periods, 100, 1,000 and 10,000 sec. Source combinations of $\{a_1\hat{\mathbf{S}}(45°, 45°), \hat{\mathbf{S}}(135°, 45°), \hat{\mathbf{S}}(90°, 135°)\}$, where a_1 is $10^{-0.5}$, and $\{\hat{\mathbf{S}}_{\zeta'}, \hat{\mathbf{S}}_{\eta'}, \hat{\mathbf{S}}_{\xi'}\}$ were used. As shown in Figure 7b, the F-norm deviations of all five sites are significantly small, at the level between 10^{-5} and 10^{-3}. However, the results changed dramatically when the 3-D anomaly was introduced. As shown in Figure 7c, the F-norm deviations calculated at two sites (L04 and L05) near the edge of the anomaly were several orders of magnitude larger than those at a site (L03) far from the boundary. These large deviations exceeded the typical observation error level of 0.01.

The modeling results, together with those of the oceanic model, suggest that the spherical MT impedances estimated from the three independent sources are non-unique when the structure is laterally heterogeneous (See also Figure S8).

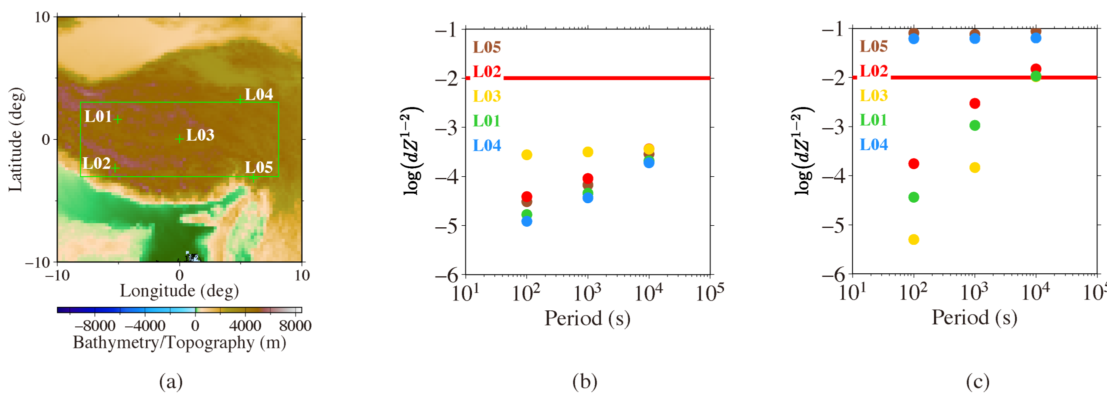

Figure 7. (a) A map showing the study region and site locations of the continental model. Green crosses show the five selected sites (Yang et al., 2020). Green rectangle shows the location of the 3-D anomaly. (b) The F-norm deviations of the spherical impedances with source combinations of $\{a_1\hat{\mathbf{S}}(45°, 45°), \hat{\mathbf{S}}(135°, 45°), \hat{\mathbf{S}}(90°, 135°)\}$ where a_1 is $10^{-0.5}$ and $\{\hat{\mathbf{S}}_{\zeta'}, \hat{\mathbf{S}}_{\eta'}, \hat{\mathbf{S}}_{\xi'}\}$ at the five selected sites in the continental model (b) without a 3-D anomaly, and (c) those with a 3-D anomaly.

5 Impedance including the induction by the radial magnetic component

5.1 Tippers and impedance non-uniqueness

Thus far, we have observed that the impedance consisting of four elements, as estimated in a spherical coordinate system, is not unique but rather depends on the source amplitude. This non-uniqueness is more pronounced in areas near coastlines or boundaries of lateral heterogeneity. Such lateral contrasts in electrical conductivity are known to cause anomalous radial components of the induced magnetic field (e.g., Parkinson, 1959; Schmucker, 1970; Kruglvakov & Kuvshinov, 2022). These observations strongly suggest that induction by the radial magnetic component plays an important role in the non-uniqueness of the four elements of the MT impedance calculated in a spherical coordinate system using Eq. (28).

To further investigate the relationship between the radial magnetic component and the non-uniqueness of the impedance, we examined the behavior of tippers (geomagnetic transfer functions). Tippers describe a linear relation between the tangential and radial magnetic components as:

$$H_r = T_\theta H_\theta + T_\varphi H_\varphi + \delta\epsilon_{H_r}, \tag{29}$$

where T_θ and T_φ are the θ- and φ-components of the tipper, respectively, and $\delta\epsilon_{H_r}$ is a residual term of linear fitting. To compare two tipper vectors, we used the L2-norm deviation, defined as:

$$dT^{1-2} = \frac{\|\mathbf{T}^1 - \mathbf{T}^2\|_2}{\|\mathbf{T}^2\|_2}. \tag{30}$$

where the L2-norm of a tipper vector is given by:

$$\|\mathbf{T}\|_2 = \left\{|T_\theta|^2 + \left|T_\varphi\right|^2\right\}^{1/2}. \tag{31}$$

We also defined the averaged L2-norm deviation of tippers over the entire study region as:

$$dT_{avg}^{1-2} = \frac{1}{N}\sum_{n=1,N}\frac{\|\mathbf{T}_n^1 - \mathbf{T}_n^2\|_2}{\|\mathbf{T}_n^2\|_2}, \tag{32}$$

similar to the average F-norm deviation of the MT impedances given by Eq. (6). Superscripts 1 and 2 denote the tippers for the two-source combinations of variable amplitude factors and those for a reference source combination $\{\hat{\mathbf{S}}_{\zeta'}, \hat{\mathbf{S}}_{\eta'}, \hat{\mathbf{S}}_{\xi'}\}$, respectively.

Kruglyakov and Kuvshinov (2022) modeled tippers in a spherical coordinate system with a plane-wave treatment by creating a source that does not produce a radial magnetic component at the Earth's surface. However, the radial component of the source magnetic field does not need to vanish at the Earth's surface as long as the condition for plane-wave approximation is satisfied for the primary field; that is, the induction wavenumber dominates the source wavenumber (Utada, 2018). This condition is satisfied in the present study, given the values of electrical conductivity and the period range used in the modeling calculations. Additionally, it is not feasible to select different sources to estimate the MT impedances and tippers from the field data. Therefore, we used external dipoles, the same sources as those used to estimate impedances in Section 4 (Figure 6), for the calculation of tippers on the spherical Earth.

Figure 8 shows the numerical modeling results for the continental model (see also Figure S9), presenting the averaged L2-norm deviations of the tippers. These deviations were calculated when a_1 (represented by open black circles), a_2 (represented by solid black diamonds), and a_3 (represented by open black diamonds) varied between 10^{-5} and 10^5. Overall, the average deviation of the tippers (Figure 8) closely resembles the behavior of the impedances (Figure 6). The deviations are approximately 10^{-8} and 10^{-7} when the amplitude factor is near unity, whereas they increase sharply when the amplitude factor deviates slightly from unity. The deviations are stable at high values, ranging between 10^{-1} and 1 when the amplitude factors are smaller than 10^{-2} or larger than 10^2. Figure 8 also illustrates the behavior of Cartesian tippers (represented by solid green circles). In this case, the amplitude of the E-W source was varied from 10^{-5} to 10^5, while the amplitude of the N-S source was held constant at unity. The tippers were then evaluated and compared with those obtained when both source amplitudes were set to unity, to calculate the average deviations. The deviations of the Cartesian tippers are significantly smaller than those of the spherical tippers and remain stable at approximately 10^{-15} or smaller than 10^{-10}.

This result suggests that Cartesian tippers can be regarded as a unique EM response function, unlike spherical tippers.

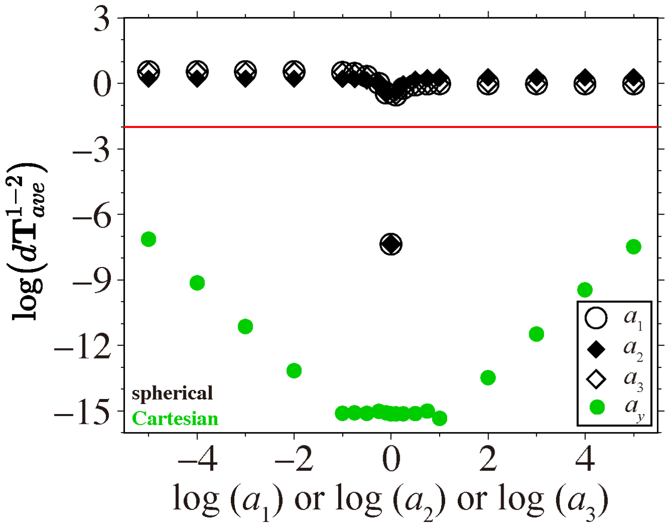

Figure 8. Dependence of dT^{1-2}_{avg} on $\log(a_1)$, $\log(a_2)$, or $\log(a_3)$ in a range when a_1, a_2, or a_3 is between $10^{-0.5}$ and $10^{0.5}$ in the entire study region at a period of 10,000 sec. Open black cirlces represent $d\mathbf{Z}^{1-2}_{avg}$ between tippers from source combination of $\{a_1\hat{\mathbf{S}}(45°, 45°), \hat{\mathbf{S}}(135°, 45°), \hat{\mathbf{S}}(90°, 135°)\}$; and from $\{\hat{\mathbf{S}}_{\zeta'}, \hat{\mathbf{S}}_{\eta'}, \hat{\mathbf{S}}_{\xi'}\}$, solid black diamonds between those from source combination of $\{\hat{\mathbf{S}}(45°, 45°), a_2\hat{\mathbf{S}}(135°, 45°), \hat{\mathbf{S}}(90°, 135°)\}$ and from $\{\hat{\mathbf{S}}_{\zeta'}, \hat{\mathbf{S}}_{\eta'}, \hat{\mathbf{S}}_{\xi'}\}$, and open black diamonds between those from $\{\hat{\mathbf{S}}(45°, 45°), \hat{\mathbf{S}}(135°, 45°), a_3\hat{\mathbf{S}}(90°, 135°)\}$, and $\{\hat{\mathbf{S}}_{\zeta'}, \hat{\mathbf{S}}_{\eta'}, \hat{\mathbf{S}}_{\xi'}\}$. Solid green circles represent deviations between 4-element Cartesian impedances (See Appendix B). Model: the continental model with a 3-D anomaly in a rotated spherical coordinate system and in a Cartesian coordinate system with the azimuthal equidistant projection (e.g., Snyder, 1987).

Figure 9a and 9b show maps of the L2-norm of tippers and the F-norm deviation of impedances for the continental model with a high conductivity anomaly and for the oceanic model, respectively. In these maps, tipper norms are obtained using a source combination of $\{\hat{\mathbf{S}}_{\zeta'}, \hat{\mathbf{S}}_{\eta'}, \hat{\mathbf{S}}_{\xi'}\}$ and impedance deviations are obtained between the impedances for the source combinations of $\{a_1\hat{\mathbf{S}}(45°, 45°), \hat{\mathbf{S}}(135°, 45°), \hat{\mathbf{S}}(90°, 135°)\}$, where a_1 is $10^{-0.5}$, and $\{\hat{\mathbf{S}}_{\zeta'}, \hat{\mathbf{S}}_{\eta'}, \hat{\mathbf{S}}_{\xi'}\}$. A strong correlation is observed between the two maps. Figures 10a and 10b display a correlation plot between the impedance deviations and tipper norms for the continental and oceanic models, respectively. Figure 10a demonstrates a clear positive correlation between the impedance deviation and tipper norm for the continental model whereas Figure 10b indicates a similar but weaker positive correlation for the oceanic model. The results from both numerical experiments suggest that the impedance deviation due to the source amplitude effect tends to increase with the tipper norm.

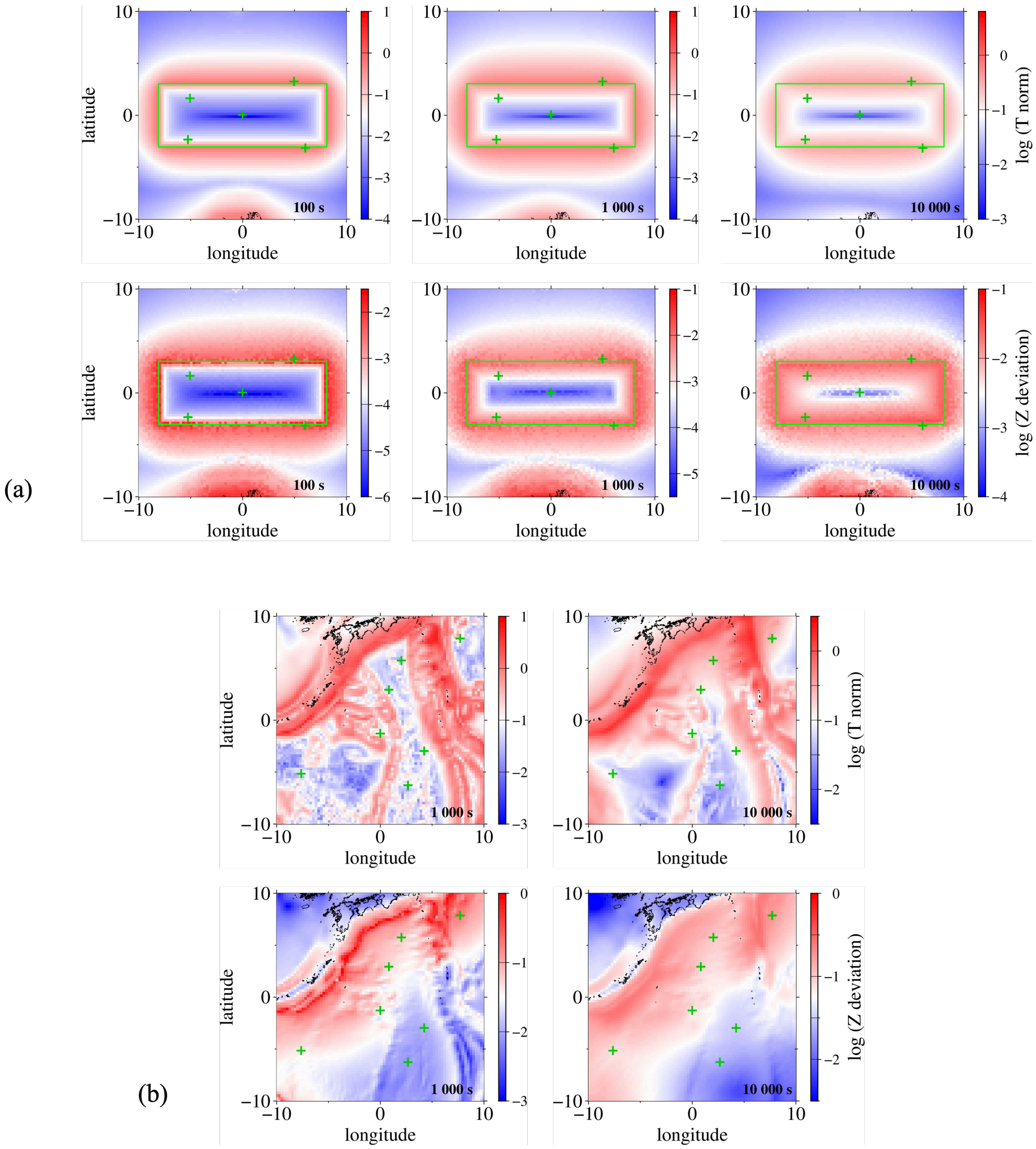

Figure 9. Top: Logarithm of tipper norms calculated with $\{\hat{\mathbf{S}}_{\zeta'}, \hat{\mathbf{S}}_{\eta'}, \hat{\mathbf{S}}_{\xi'}\}$. Bottom: Logarithm of F-norm deviations between impedances calculated from source combinations of $\{a_1\hat{\mathbf{S}}(45°, 45°),$

$\hat{\mathbf{S}}(135°, 45°)$, $\hat{\mathbf{S}}(90°, 135°)\}$ when a_1 is $10^{-0.5}$ and $\{\hat{\mathbf{S}}_{\zeta'}, \hat{\mathbf{S}}_{\eta'}, \hat{\mathbf{S}}_{\xi'}\}$. (a) for the continental model and (b) for the oceanic model, in a rotated spherical coordinate system.

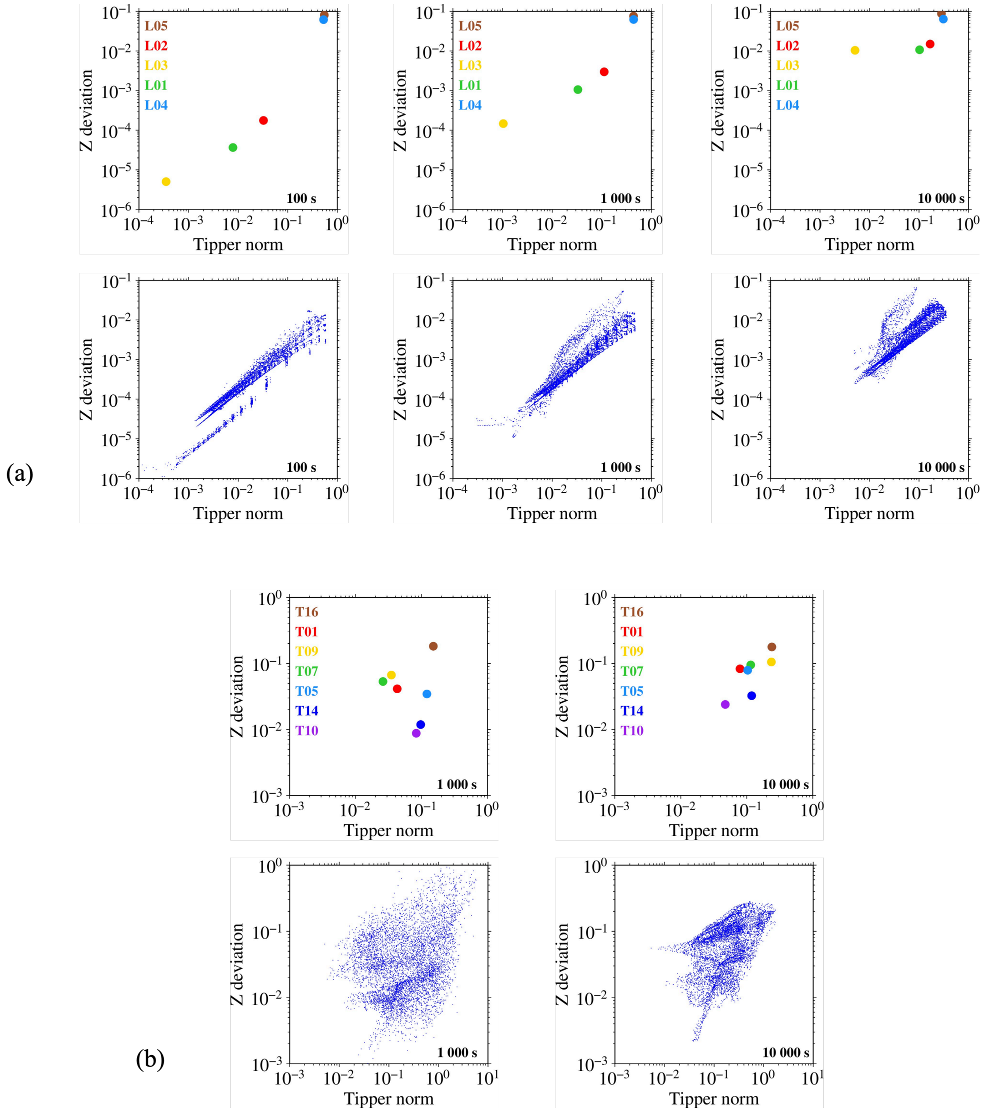

Figure 10. Dependence of F-norm impedance deviation on tipper norm at selected sites (top) and at all grid points at the surface of the Earth in the study region (bottom). Tippers are calculated from $\{\hat{\mathbf{S}}_{\zeta'}, \hat{\mathbf{S}}_{\eta'}, \hat{\mathbf{S}}_{\xi'}\}$. F-norm impedance deviations are calculated between results from $\{a_1\hat{\mathbf{S}}(45°, 45°), \hat{\mathbf{S}}(135°, 45°)$, $\hat{\mathbf{S}}(90°, 135°)\}$ where a_1 is $10^{-0.5}$ and $\{\hat{\mathbf{S}}_{\zeta'}, \hat{\mathbf{S}}_{\eta'}, \hat{\mathbf{S}}_{\xi'}\}$, (a) for the continental model and (b) for the oceanic model, in a rotated spherical coordinate system.

5.2 6-element spherical impedance

The positive correlation between the impedance deviation and tipper norm obtained in the previous section strongly suggests that the radial component of the magnetic field (both source and induced) contributes to the non-uniqueness of the spherical impedance. Based on these findings and a simple theoretical consideration of the impedance when the primary field includes a vertical component (Appendix A), we introduced a new MT impedance in a spherical model that accounts for induction by the radial magnetic component.

In general, the linear relation between three components of the electric and magnetic fields in a conductive medium is expressed by a complex-valued 3 × 3 impedance tensor. Since the radial component of the electric field diminishes at the surface of the Earth, the new MT impedance $\mathbf{Z}^U$ becomes a complex-valued 2 × 3 matrix. This impedance can be determined by solving a linear equation relating the EM components from three independent sources:

$$\begin{pmatrix} E_\theta^1 & E_\theta^2 & E_\theta^3 \\ E_\varphi^1 & E_\varphi^2 & E_\varphi^3 \end{pmatrix} = \begin{pmatrix} Z_{\theta\theta}^U & Z_{\theta\varphi}^U & Z_{\theta r}^U \\ Z_{\varphi\theta}^U & Z_{\varphi\varphi}^U & Z_{\varphi r}^U \end{pmatrix} \begin{pmatrix} H_\theta^1 & H_\theta^2 & H_\theta^3 \\ H_\varphi^1 & H_\varphi^2 & H_\varphi^3 \\ H_r^1 & H_r^2 & H_r^3 \end{pmatrix}. \tag{33}$$

Hereafter, we refer to the new impedance with symbol U as the 6-element spherical impedance, where the notation with superscript U distinguishes it from the spherical impedance consisting of four elements (hereafter referred to as the 4-element impedance) calculated using Eq. (26) or (28). Dmitriev and Berdichevsky (2002) proposed the 6-element impedance in a Cartesian model and named it a generalized impedance. They introduced a method to calculate the impedance using 3-D Cartesian forward modeling, although no calculation results have been reported thus far.

Figure 11 presents the apparent resistivities and impedance phases at site T16 in the oceanic model, which is the site nearest to the coastline. The results from the 4-element spherical impedances for $\{\hat{\mathbf{S}}_{\zeta'}, \hat{\mathbf{S}}_{\eta'}\}$ (represented by solid red triangles) or $\{\hat{\mathbf{S}}_{\zeta'}, \hat{\mathbf{S}}_{\eta'}, \hat{\mathbf{S}}_{\xi'}\}$ (represented by open green squares), as well as those from the 6-element spherical impedance for $\{\hat{\mathbf{S}}_{\zeta'}, \hat{\mathbf{S}}_{\eta'}, \hat{\mathbf{S}}_{\xi'}\}$ (represented by solid blue circles) are shown. The results indicate that apparent resistivities calculated from $Z_{\theta r}^U$ and $Z_{\varphi r}^U$ are of a similar order of magnitude to those estimated from the other four elements.

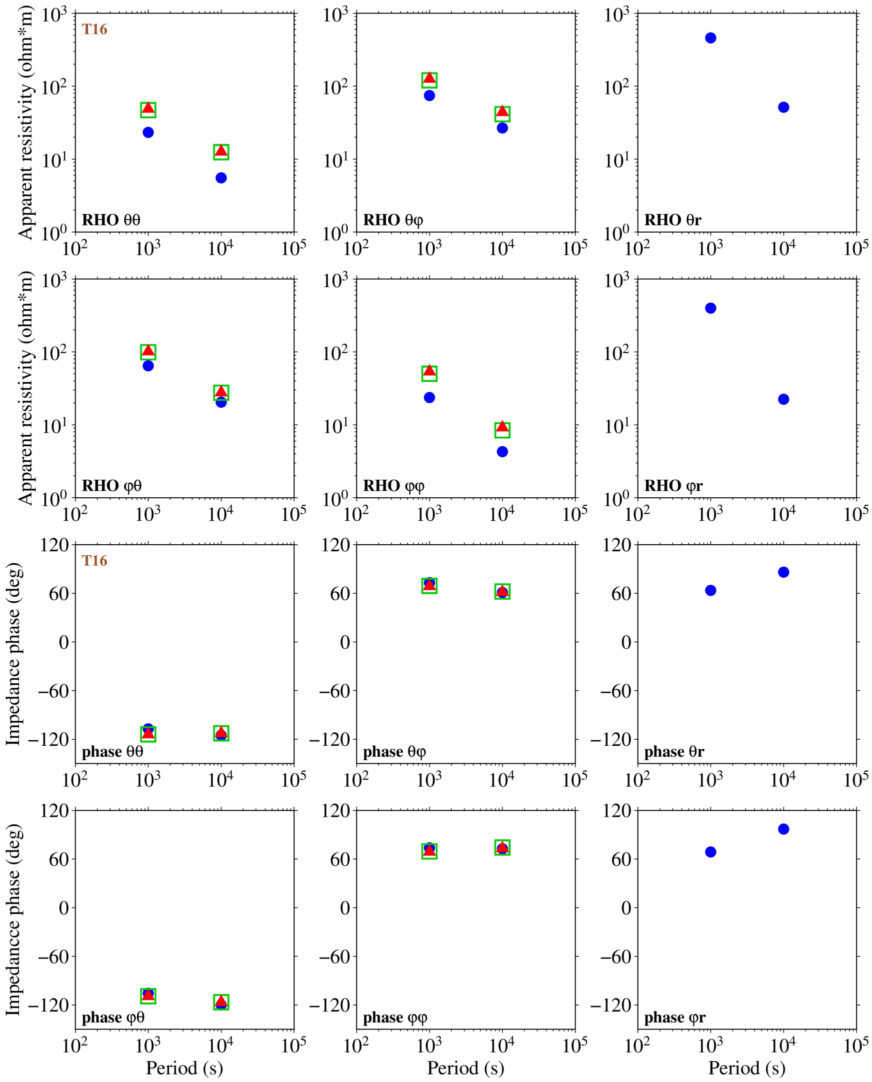

Figure 11. Period dependance of apparent resistivities and impedance phases at T16. Solid red triangles: 4-element impedances from $\{\hat{\mathbf{S}}_{\zeta'}, \hat{\mathbf{S}}_{\eta'}\}$; open green squares: 4-element impedances from $\{\hat{\mathbf{S}}_{\zeta'}, \hat{\mathbf{S}}_{\eta'}, \hat{\mathbf{S}}_{\xi'}\}$; solid blue circles: 6-element impedances from $\{\hat{\mathbf{S}}_{\zeta'}, \hat{\mathbf{S}}_{\eta'}, \hat{\mathbf{S}}_{\xi'}\}$. Model: the oceanic model in a rotated spherical coordinate system.

The source amplitude dependence of the estimated impedances in the oceanic model was further examined using the source combinations $\{a_1\hat{\mathbf{S}}(45°, 45°), \hat{\mathbf{S}}(135°, 45°), \hat{\mathbf{S}}(90°, 135°)\}$, $\{\hat{\mathbf{S}}(45°, 45°), a_2\hat{\mathbf{S}}(135°, 45°), \hat{\mathbf{S}}(90°, 135°)\}$ and $\{\hat{\mathbf{S}}(45°, 45°), \hat{\mathbf{S}}(135°, 45°), a_3\hat{\mathbf{S}}(90°, 135°)\}$, which are the same source combinations used in Section 4 (Figure 6). The 6-element impedance from a combination of the three basis sources was used as the reference. Figure 12 shows the averaged F-norm deviations of the 6-element spherical impedances obtained when each value of the amplitude factor a_1 (represented by open black circles), a_2 (represented by solid black diamonds), or a_3 (represented by open black diamonds) was varied from 10^{-5} to 10^5. The deviations are on the order of 10^{-14} when the amplitude factors are near unity and remain below 10^{-5} across the entire range of amplitude factors examined, which can be considered as sufficiently small compared with the target level of 0.01. Considering that the convergence criterion in our numerical calculation was set to 10^{-16}, deviations on the order of 10^{-14} can be attributed to the accumulated numerical errors. Therefore, the 6-element spherical impedance can be regarded as essentially unique.

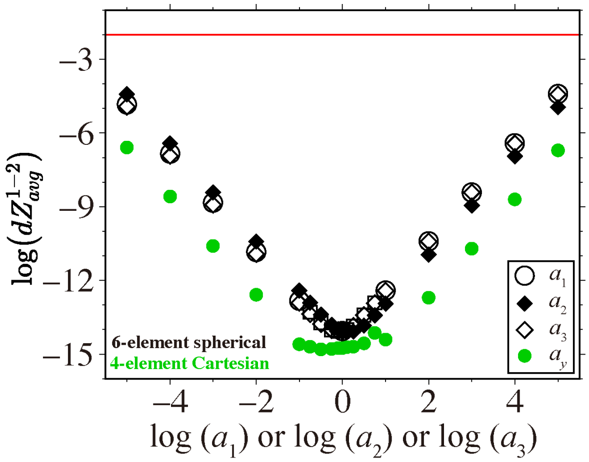

Figure 12. Dependence of dZ_{avg}^{1-2} on $\log(a_1)$, $\log(a_2)$, or $\log(a_3)$ in a range when a_1, a_2, or a_3 is between 10^{-5} and 10^{5} in the entire study region at period of 10,000 sec. Open black circles represent averaged deviations between 6-element impedances from source combinations $\{a_1\hat{\mathbf{S}}(45°, 45°), \hat{\mathbf{S}}(135°, 45°), \hat{\mathbf{S}}(90°, 135°)\}$, and $\{\hat{\mathbf{S}}_{\zeta'}, \hat{\mathbf{S}}_{\eta'}, \hat{\mathbf{S}}_{\xi'}\}$, solid black diamonds between those from $\{\hat{\mathbf{S}}(45°, 45°), a_2\hat{\mathbf{S}}(135°, 45°), \hat{\mathbf{S}}(90°, 135°)\}$ and $\{\hat{\mathbf{S}}_{\zeta'}, \hat{\mathbf{S}}_{\eta'}, \hat{\mathbf{S}}_{\xi'}\}$, and open black diamonds between those from $\{\hat{\mathbf{S}}(45°, 45°), \hat{\mathbf{S}}(135°, 45°), a_3\hat{\mathbf{S}}(90°, 135°)\}$, and $\{\hat{\mathbf{S}}_{\zeta'}, \hat{\mathbf{S}}_{\eta'}, \hat{\mathbf{S}}_{\xi'}\}$. Solid green circles represent deviations between 4-element Cartesian impedances (See Appendix B). Model: the oceanic model in a rotated spherical coordinate system and in a Cartesian coordinate system with the azimuthal equidistant projection.

Results of similar numerical experiments in a Cartesian coordinate system are represented by solid green circles in Figure 12 (See Appendix B for details). These results demonstrate that the level of uniqueness of the 6-element spherical impedance is comparable to that of the 4-element Cartesian impedance. We conclude that both the 4-element Cartesian impedance and the 6-element spherical impedance are independent of the source amplitude and can be employed as EM response functions.

6 Discussion

The 4- and 6-element spherical impedances are examined numerically in Sections 4 and 5, respectively. In Section 5, we found that tippers and 4-element impedances are related. Here we demonstrate that tipper plays an important role in causing the non-uniqueness of the 4-element impedance. The 6-element impedance $\mathbf{Z}^U$ in Eq. (33) can be substituted into the 4-element impedance $\mathbf{Z}$ in Eq. (26) using the tipper components T_θ and T_φ in Eq. (29). Substituting Eq. (29) into Eq. (33), while ignoring the residual term $\delta\epsilon_{H_r}$, we can approximately express the 4-element impedance in terms of the 6-element impedance and tippers as

$$Z_{\theta\theta} \approx Z_{\theta\theta}^U + Z_{\theta r}^U T_\theta, \tag{34}$$

$$Z_{\theta\varphi} \approx Z_{\theta\varphi}^U + Z_{\theta r}^U T_\varphi, \tag{35}$$

$$Z_{\varphi\theta} \approx Z_{\varphi\theta}^{U} + Z_{\varphi r}^{U} T_{\theta}, \tag{36}$$

and

$$Z_{\varphi\varphi} \approx Z_{\varphi\varphi}^{U} + Z_{\varphi r}^{U} T_{\varphi}. \tag{37}$$

Dmitriev and Berdichevsky (2002) derive a similar relationship in a Cartesian coordinate system.

This relationship can account for certain properties of the 4-element spherical impedance, particularly its non-uniqueness, because the 6-element spherical impedance is shown to be unique, while the tippers are not. More precisely, the 4-element spherical impedance is not a unique response of the Earth's conductivity structure but exhibits considerable source amplitude dependence unless the Earth's structure is nearly 1-D (laterally uniform), where the tippers are negligible so that the second terms on the right-hand side of Eqs. (34)–(37) are also negligible.

As an application of this relationship, we consider seasonal variations in tippers and MT impedances, which have been documented in different land regions across a wide range of periods (e.g., Kappler et al., 2010; Brändlein et al., 2012; Araya et al., 2013; Ernst et al., 2020, 2022). Ernst et al. (2020, 2022) reported that seasonal variations in tippers were more significant than those in 4-element impedances, attributing this to variations of the external radial (vertical) magnetic component. Based on this observation and considering the role of tippers in connecting the 6-element to the 4-element spherical impedance (Eqs. (34)–(37)), it would be valuable to examine the behavior of tippers for different amplitudes of the radial component of the source fields in spherical models. In this study, we used a continental model with one 3-D anomaly (Figure 7) because this model exhibits a simple and clear pattern with large tippers only near the boundaries of the lateral conductivity contrasts (Figure 9).

We examined tippers with the source combination $\{\hat{\mathbf{S}}_{\zeta'}, \hat{\mathbf{S}}_{\eta'}, a_{\xi'}\hat{\mathbf{S}}_{\xi'}\}$ and $\{\hat{\mathbf{S}}_{\zeta'}, a_{\eta'}\hat{\mathbf{S}}_{\eta'}, \hat{\mathbf{S}}_{\xi'}\}$, where the amplitude factors $a_{\xi'}$ and $a_{\eta'}$ were set to 1, 2, 5, or 10. This test allows us to separately analyze the influence of the radial and tangential components of the external magnetic fields on the tippers. We selected site L04, located near the northern edge of the conductivity contrast, where significant amplitudes of the tippers were expected (Figure 9a). The calculated tipper amplitude showed a tendency to increase with $a_{\xi'}$ (Figure 13a). However, changes in T_{φ} is more pronounced than those in T_{θ}. This tendency is opposite to the observation by Ernst et al. (2020), where variations in T_{θ} were larger than those in T_{φ}. In contrast, variations in the tippers when $a_{\eta'}$ was varied (Figure 13b) were significantly smaller than those observed for variations in $a_{\xi'}$ (Figure 13a). Based on these results, we focused on the case of varying $a_{\xi'}$, which corresponds to the influence of changes in the radial magnetic component of the external field.

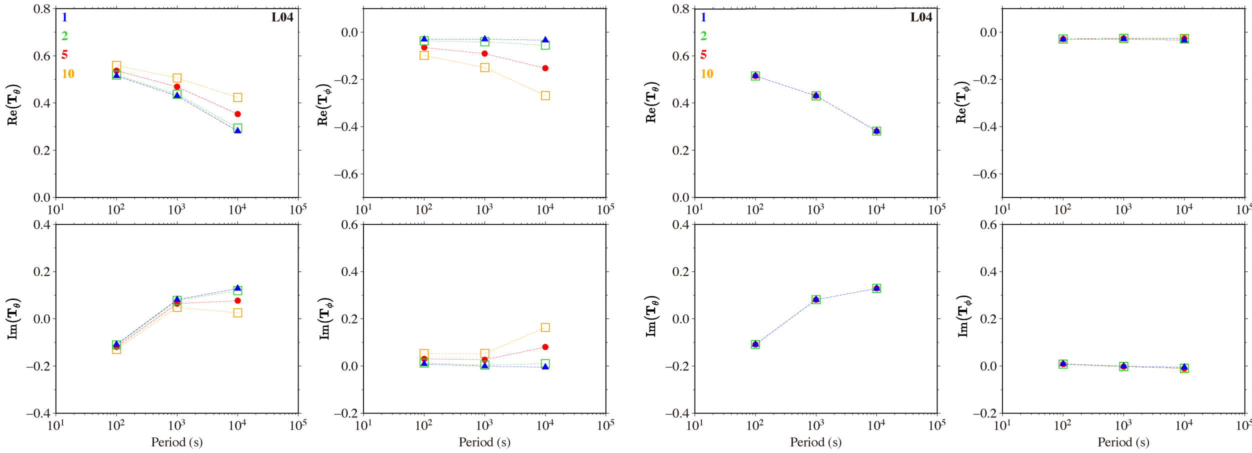

(a) (b)

Figure 13. Dependence of tipper on period at site L04 when amplitudes (a) $a_{\xi'}$ in $\{\hat{\mathbf{S}}_{\zeta'}, \hat{\mathbf{S}}_{\eta'}, a_{\xi'}\hat{\mathbf{S}}_{\xi'}\}$ or (b) $a_{\eta'}$ in $\{\hat{\mathbf{S}}_{\zeta'}, a_{\eta'}\hat{\mathbf{S}}_{\eta'}, \hat{\mathbf{S}}_{\xi'}\}$ has different values. Blue solid triangles, green open squares, red solid circles, and orange open squares indicate results when the source amplitude $a_{\xi'}$ or $a_{\eta'}$ is 1, 2, 5 and 10, respectively. Model: the continental model with a 3-D anomaly in a rotated spherical coordinate system.

Figure 14a shows the difference in tippers observed by Ernst et al. (2020), who calculated the absolute seasonal differences between tippers estimated from the magnetic field data in summer and winter (represented by black solid circles). Additionally, the absolute differences in the real and imaginary parts between two tippers, which were calculated in this study with various $a_{\xi'}$ and those with $a_{\xi'} = 1$ at L04, are shown in Figure 14a. We found that the seasonal changes in the real and imaginary parts of T_θ reported by Ernst et al. (2020) can be roughly explained by a change in the amplitude of the source radial magnetic component between 1 (at shorter periods) and 9 (at longer periods) and those of T_φ can be explained by a smaller change, approximately 1. Although fitting the continental model results to the observations of Ernst et al. (2020) is not the main aim of this study, these findings suggest that the magnitude of seasonal variations in tippers can be explained by varying the amplitude of the external radial magnetic component using only degree-one (spatially uniform) sources.

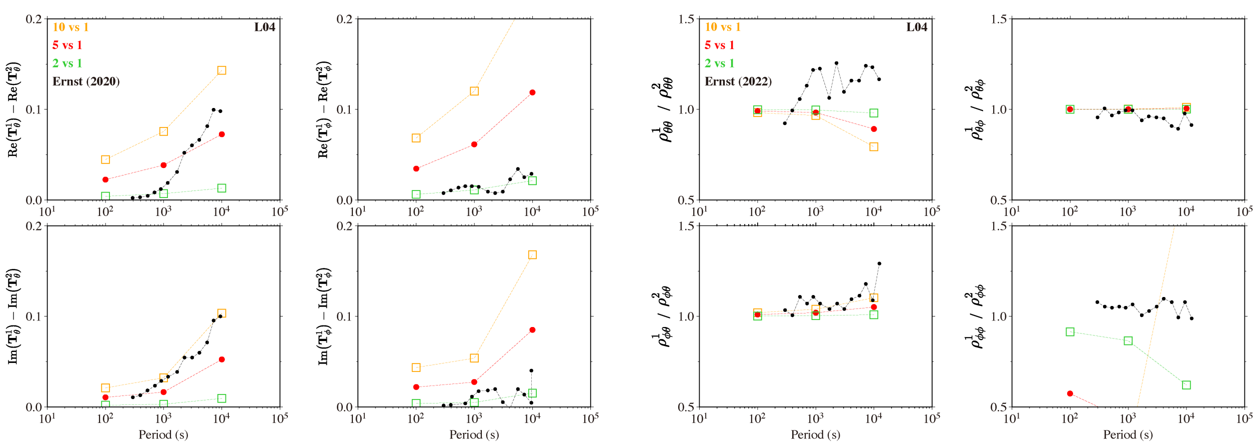

(a) (b)

Figure 14. Period dependence of (a) absolute differences in tipper norm and (b) apparent resistivity at L04 for different values of the source amplitude ($a_{\xi'}$=1, 2, 5 or 10). Model: the continental model with a 3-D anomaly in a rotated spherical coordinate system.

We further examined the apparent resistivity differences at site L04 for varying $a_{\xi'}$ values and compared them to those obtained from observed data by Ernst et al. (2022) as shown in Figure 14b. Differences of approximately 0.01 in $\rho_{a_{\varphi\theta}}$ and 0.1 in $\rho_{a_{\theta\varphi}}$ at a period of 10,000 sec at L04 could be attributed to a case where $a_{\xi'} \approx 10$. A more detailed discussion of the amplitude differences between the sources requires the use of a more realistic model of electrical conductivity below the study area in Europe. We also suggest that examining six elements of the impedance, rather than four, would better capture time-dependent changes in the Earth's electrical conductivity. This is because the 6-element impedance is independent of the source amplitude, so far as only external dipoles are considered.

To gain deeper insights into the uniqueness and non-uniqueness of the 6- and 4-element spherical impedances, we analyzed cases where one of the amplitude factors (a1a_1a1, a2a_2a2, or a3a_3a3) of the three independent sources was varied (Figure 12). For the 6-element impedance, the average deviation remained nearly constant at a negligibly small value (~10^{-14}) when the amplitude factor ranged between 10^{-1} and 10^{1} (Figure 12). In contrast, we observe a gradually increasing trend in the average deviation when the amplitude factor is smaller than 10^{-1} or larger than 10^{1} (Figure 12). This occurs because the amplitude of one of the three orthogonal sources is significantly smaller or greater than that of the other two, accumulating rounding errors in solving Eq. (33) for the six impedance elements. Nevertheless, acceptable solutions were still obtained within a wide amplitude range of 10^{-5} to 10^{5} (Figure 12). These results indicate that estimating unique values of the 6-element impedances is stable and feasible for most combinations of the three external dipole sources over a broad amplitude range.

In contrast, in the case of 4-element spherical impedance, we observed a sudden and significant increase in the F-norm deviations when the amplitude factor of one of the three independent sources slightly deviated from unity (Figure 6). Figure 15 shows the detailed behavior of the deviations for the ranges of a_1, a_2, and a_3 corresponding to the hatched interval in Figure 6. The deviations continued to increase for amplitudes decreasing from unity to 10^{-1} or increasing from unity to 10^{1}, and then remained nearly stable at values between 0.01 and 1 for further decreasing or increasing amplitudes (Figure 6). This behavior suggests that unique estimation of the 4-element spherical impedances may be possible, but only under limited condition where the given sources to be decomposed into three orthogonal sources with nearly equal amplitudes. However, the minimum deviation of the 4-element impedance is notably larger than that of the 6-element impedance.

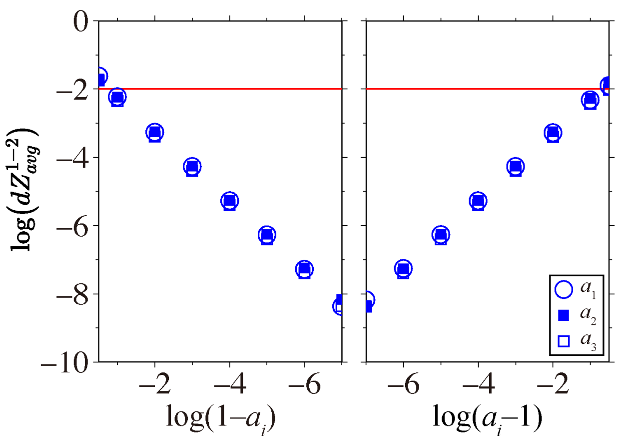

Figure 15. Dependence of dZ_{avg}^{1-2} on log(1–a_i) or log(a_i–1) (i=1, 2 or 3) in a range between –7 and –0.5 (hatched area in Figure 6) in the whole study region at period of 10,000 sec. Symbols are the same with Figure 6. Model: the oceanic model in a rotated spherical coordinate system.

Note that the residual terms in Eq. (28) of the overdetermined problem to estimate the 4-element impedance are significant. Here, we define the averaged residual across the entire study region for the external source k as:

$$d\boldsymbol{\epsilon}_{\mathbf{E}}^{k} = \frac{1}{N} \sum_{n=1,N} \frac{\left\| \delta \boldsymbol{\epsilon}_{\mathbf{E}}^{k} \right\|_2}{\left\| \mathbf{E}^{k} \right\|_2}, \tag{38}$$

where subscript n represents a calculation cell in the study region, and N is the total number of cells for the oceanic model or the continental model. For a source combination of $\{\hat{\mathbf{S}}_{\zeta'}, \hat{\mathbf{S}}_{\eta'}, \hat{\mathbf{S}}_{\xi'}\}$, the average residuals for the three sources are listed in Table 1 for two periods. We noticed relatively large residuals for $\hat{\mathbf{S}}_{\xi'}$, indicating the significant influence of ignoring the induction by the radial magnetic components when calculating the 4-element impedance. The effects of induction by the radial magnetic component are incorporated into the four elements through the linear relationships in Eqs. (34)–(37). As a result, the impedance relation expressed using the 4-element impedance is inaccurate, particularly for $\hat{\mathbf{S}}_{\xi'}$ which generates a source field oriented nearly in the radial direction within the study region (Table 1). This explains why the deviation of the 4-element impedance cannot be as small as that of the 6-element impedance, even when three basis sources are given.

Table 1

Averaged residuals $\mathrm{d}\boldsymbol{\epsilon}_{\mathbf{E}}^{\mathrm{k}}$ *when calculating 4-element impedances from the source combination of* $\{\hat{\mathbf{S}}_{\zeta'}, \hat{\mathbf{S}}_{\eta'}, \hat{\mathbf{S}}_{\xi'}\}$. *Model: oceanic model in the rotated spherical coordinate system.*

Source	T = 1,000 s	10,000 s
$\hat{\mathbf{S}}_{\zeta'}$	0.0112	0.0080
$\hat{\mathbf{S}}_{\eta'}$	0.0121	0.0090
$\hat{\mathbf{S}}_{\xi'}$	0.5837	0.6174

The source effect discussed thus far is observed only in the 4-element spherical impedance, which we call the "source amplitude effect." In general, any source combination can be decomposed into three basis sources with specific amplitude factors. The source amplitude effect in 4-element spherical impedance arises when the amplitude factors of decomposed three orthogonal sources are unequal. However, questions remain, such as how significant the non-uniqueness of the 4-element spherical impedance is and whether estimating the 6-element spherical impedance is necessary in practice. Further investigation is required to address these questions. Once the validity of using the 6-element impedance is established, both modeling and inversion of MT observational data should be conducted in a spherical coordinate system rather than in a Cartesian coordinate system.

Another type of source effect is known to exist, which affects both the 4- and 6-element spherical impedances. We refer to this as the "source harmonic degree effect", caused by sources with different harmonic degrees. This type of source effect similarly manifests in the Cartesian MT impedance as the source wavenumber effect, also known as the source dimension effect (see Appendix A). The large impedance residual for the source $\hat{\mathbf{S}}_{\xi'}$, which increases with period (Table 1), can be partially attributed to this effect. While addressing how to properly account for this effect at higher harmonic degrees in a spherical coordinate system is an important problem, it is beyond the scope of this study.

7 Conclusions

In this study, we conducted systematic MT modeling in a spherical coordinate system, using laterally heterogeneous oceanic and continental models to examine the effects of source polarization and amplitude on the MT impedance. Our results revealed that the 4-element spherical impedance, estimated from two independent sources, is non-unique and exhibits considerable dependence on source polarization and amplitude, unless the Earth's structure is nearly 1-D. When three independent sources are applied, the 4-element spherical impedance no longer exhibits a source polarization effect; however, source amplitude dependence persists. We observed that the non-uniqueness in the 4-element spherical impedance is positively correlated with the tipper norm. Based on this observation and a simple theoretical consideration (Appendix A), we introduced a new impedance model consisting of six elements, which incorporates induction by the radial magnetic components. Our findings demonstrated that the 6-element spherical impedance can be uniquely estimated, independent of the amplitude of three independent dipole sources. However, tippers remain non-unique even when three independent sources are applied. Furthermore, we established that the 6-element impedance can be related to the 4-element impedance through tippers. This relationship provides potential explanations for observed seasonal variations in tippers and 4-element impedances, which may result from variations in the amplitudes of the radial components of the external magnetic field. The 6-element impedance is a unique function only of the Earth's conductivity structure and frequency, and it is independent of the source amplitude. Therefore, the 6-element impedance is expected to serve as a more reliable EM response function for inverting the field data.

Appendix A

Impedance relation including the source wavenumber for a uniform half-space

Here, we address the solution of the EM induction equation in a Cartesian coordinate system with the origin at the Earth's surface. We consider the behavior of the primary EM field within a uniform half-space (conductivity σ) in response to the incidence of an external magnetic field polarized in the x-z plane with wavenumber ν and angular frequency ω, where z points verticaly downward. At the surface ($z = 0$) and within the Earth, two components of the magnetic field (H_x and H_z) and one component of the electric field (E_y) can be expressed as (e.g., Utada, 2018):

$$H_x(x,\omega) = \frac{i\nu\gamma}{\mu_0}\epsilon_1(\nu,\omega)e^{-\gamma z}e^{i\nu x}, \tag{A1}$$

$$H_z(x,\omega) = \frac{i\nu^2}{\mu_0}\epsilon_1(\nu,\omega)e^{-\gamma z}e^{i\nu x}, \tag{A2}$$

and

$$E_y(x,\omega) = -\omega\nu\epsilon_1(\nu,\omega)e^{-\gamma z}e^{i\nu x}, \tag{A3}$$

where ϵ_1 is a coefficient to be determined by applying a boundary condition at the surface, μ_0 is the magnetic permeability, and $\gamma = \sqrt{\nu^2 + i\omega\sigma\mu_0}$. The impedance relation for E_y can be obtained from Ampere's law as:

$$\begin{aligned} E_y(x,\omega) &= \left(\frac{1}{\sigma}\frac{\partial}{\partial z}\right)H_x(\nu,\omega) - \left(\frac{1}{\sigma}\frac{\partial}{\partial x}\right)H_z(\nu,\omega) \\ &= Z_{yx}^U(\nu,\omega)\cdot H_x(\nu_x,\omega) + Z_{yz}^U(\nu,\omega)\cdot H_z(\nu,\omega). \end{aligned} \tag{A4}$$

Using (A1)–(A4), we derive the expressions for the yx- and yz-elements of the MT impedance as follows:

$$Z_{yx}^U(\nu,\omega) = \frac{1}{\sigma}\frac{\partial H_x(\nu,\omega)}{\partial z}\Big/ H_x(\nu,\omega) = -\frac{\gamma}{\sigma} \tag{A5}$$

and

$$Z_{yz}^U(\nu,\omega) = -\frac{1}{\sigma}\frac{\partial H_z(\nu,\omega)}{\partial x}\Big/ H_z(\nu,\omega) = \frac{-i\nu}{\sigma}. \tag{A6}$$

If the combination of ω and σ satisfies the condition for the plane-wave approximation ($\nu^2 \ll |i\omega\sigma\mu_0|$), Z_{yz}^U vanishes and Z_{yx}^U approaches the well-known expression of the MT impedance first presented by Cagniard (1953). Note that Z_{yz}^U is purely imaginary because it is caused by eddy currents.

Price (1962) derived an MT impedance element Z_{yx}^P directly from Eqs. (A1) and (A3):

$$Z_{yx}^P(\nu,\omega) = \frac{E_y(x,\omega)}{H_x(\nu,\omega)} = \frac{i\omega\mu_0}{\gamma}. \tag{A7}$$

This expression is mathematically correct but not physically consistent, as it combines two induced electric fields arising from different mechanisms.

Appendix B

MT modeling in a Cartesian coordinate system

The source effects in a Cartesian coordinate system were examined by forward modeling using the ModEM code, which employed the finite difference method (Egbert & Kelbert, 2012). In this code, two uniform external source fields polarized in the N-S and E-W directions are assigned at the top boundary (1629 km in altitude) of the model domain.

We adopted a nearly identical grid spacing for both the spherical and Cartesian modeling studies, as well as for both the oceanic and continental models, to facilitate the comparison. For numerical modeling in a Cartesian coordinate system, the grid design of the two shallowest layers is the same as that in the spherical modeling, except for grids near the seafloor. To accurately estimate the MT impedance at the seafloor in the oceanic model, where there is a significant contrast in electrical conductivity between the layers above and below, 13 additional grids with denser spacing were employed near the seafloor. Such treatment was necessary because the ModEM code interpolates the magnetic field components from values at grids above and below the seafloor, whereas the spherical code extrapolates values from two grids below the seafloor (Tada et al., 2012). We confirmed that Cartesian and spherical solutions give consistent estimates of the MT impedance for a 1-D case (See Figure S3). The vertical grid spacing near the seafloor is also confirmed to be sufficiently fine for a 3-D model (See Figure S3).

The horizontal size of the Cartesian modeling domain was set to 10 007.538 6 km × 10 007.538 6 km (~ 40° × 40°). The horizontal grid spacing was set to 27.7 987 km (~ 0.25°) in the study region and gradually widened to 111.1 949 km (~ 1°), 222.3 898 km (~ 2°), and 555.9 745 km (~ 5°), depending on the distance from the study region. In total, there were 84 grid points in the z-direction and 176 grid points in both the x- and y-directions.

Here, we present numerical results from three experiments to demonstrate that the Cartesian impedance is independent of both source polarization and amplitude, using the oceanic model. Note that the calculated impedance elements were converted to those in the original coordinate system for consistency with an actual field measurement. The position vector at any location is defined by $\mathbf{r} = (x, y, z)^t$, where x, y, and z denote the geographical northward, eastward, and downward directions, respectively. The superscript t denotes the transpose. The azimuthal equidistant projection (e.g., Snyder, 1987) is employed for the map projection.

Let a plane-wave source with arbitrary polarization and amplitude in the Cartesian coordinate system be denoted as $\mathbf{S}(\gamma_\mathbf{S})$, where the azimuth $\gamma_\mathbf{S}$ represents the angle from the x-direction (Figure B1). The source $\mathbf{S}(\gamma_\mathbf{S})$ can be decomposed into two basis sources as:

$$\mathbf{S}(\gamma_\mathbf{S}) = a_x\hat{\mathbf{S}}_x + a_y\hat{\mathbf{S}}_y, \tag{B1}$$

where a_x and a_y are amplitude factors. By normalizing $\mathbf{S}$, we can derive a plane-wave source of unit amplitude with arbitrary polarization as:

$$\hat{\mathbf{S}}(\gamma_\mathbf{S}) = \hat{a}_x\hat{\mathbf{S}}_x + \hat{a}_y\hat{\mathbf{S}}_y, \tag{B2}$$

where

$$\hat{a}_x = \frac{a_x}{|\mathbf{S}(\gamma_\mathbf{S})|} = \cos(\gamma_\mathbf{S}) \tag{B3}$$

and

$$\hat{a}_y = \frac{a_y}{|\mathbf{S}(\gamma_\mathbf{S})|} = \sin(\gamma_\mathbf{S}). \tag{B4}$$

Let the external magnetic field due to an arbitrary source $\mathbf{S}(\gamma_\mathbf{S})$ in a Cartesian coordinate system be denoted as $\mathbf{H}_{ext}(\mathbf{r}, \omega, \mathbf{S})$. Using Eq. (B1) and the linearity of the EM field, we derive:

$$\mathbf{H}_{ext}(\mathbf{r}, \omega, \mathbf{S}) = a_x \mathbf{H}_{ext}(\mathbf{r}, \omega, \hat{\mathbf{S}}_x) + a_y \mathbf{H}_{ext}(\mathbf{r}, \omega, \hat{\mathbf{S}}_y). \tag{B5}$$

The solution of Maxwell's equations, $\mathbf{E}(\mathbf{r}, \omega, \mathbf{S})$ and $\mathbf{H}(\mathbf{r}, \omega, \mathbf{S})$, for an arbitrary source $\mathbf{S}(\gamma_\mathbf{S})$ in a Cartesian coordinate system can then be obtained as linear combinations of the solutions for two basis sources:

$$\mathbf{E}(\mathbf{r}, \omega, \mathbf{S}) = a_x \mathbf{E}(\mathbf{r}, \omega, \hat{\mathbf{S}}_x) + a_y \mathbf{E}(\mathbf{r}, \omega, \hat{\mathbf{S}}_y), \tag{B6}$$

and

$$\mathbf{H}(\mathbf{r}, \omega, \mathbf{S}) = a_x \mathbf{H}(\mathbf{r}, \omega, \hat{\mathbf{S}}_x) + a_y \mathbf{H}(\mathbf{r}, \omega, \hat{\mathbf{S}}_y). \tag{B7}$$

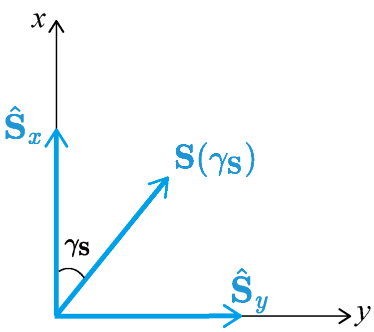

Figure B1. External sources in the Cartesian coordinate system. **S** is a source of arbitrary polarization (azimuth $\gamma_\mathbf{S}$) and amplitude.

Here we have tested three cases. In Case 1, the polarizations of two orthogonal sources were changed by the same angle $\gamma_\mathbf{S}$ to calculate $\mathbf{E}(\mathbf{r}, \omega, \mathbf{S})$ and $\mathbf{H}(\mathbf{r}, \omega, \mathbf{S})$. The external source combination in this case was $\{\hat{\mathbf{S}}(\gamma_\mathbf{S}), \hat{\mathbf{S}}(\gamma_\mathbf{S} + 90°)\}$, where $\gamma_\mathbf{S}$=22.5°, 45°, and 67.6°. The resulting impedances were compared with those for the source combination $\{\hat{\mathbf{S}}(0°), \hat{\mathbf{S}}(90°)\}$ to calculate the averaged deviation across the entire study region. As shown in Figure B2, the averaged deviation is consistently between 10^{-14} and 10^{-15}, suggesting that the Cartesian impedance is unique and independent of the polarizations of the two sources.

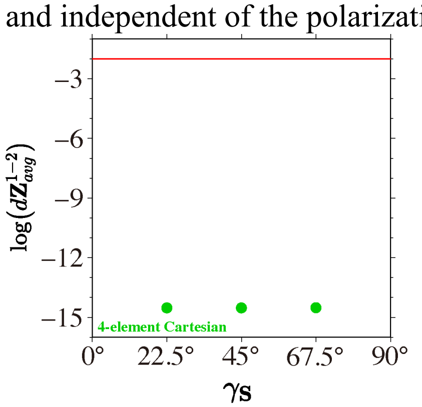

Figure B2. Dependence of dZ_{avg}^{1-2} on $\gamma_{\mathbf{S}}$ when $\gamma_{\mathbf{S}}$=22.5°, 45°, and 67.5° in the entire study region at a period of 10,000 sec. Model: Cartesian oceanic model with azimuthal equidistant projection method.

In Case 2, the polarization of only one external source was changed, resulting in two sources that were not orthogonal. The external source combination is denoted as $\{\hat{\mathbf{S}}_x, \hat{\mathbf{S}}(\gamma_{\mathbf{S}})\}$, which can also be expressed as $\{\hat{\mathbf{S}}_x, \cos(\gamma_{\mathbf{S}})\hat{\mathbf{S}}_y + \sin(\gamma_{\mathbf{S}})\hat{\mathbf{S}}_y\}$ by definition. The results shown in Figure B3 suggest that the Cartesian impedance is unique unless $\gamma_{\mathbf{S}}$ is nearly equal to zero, i.e., unless the two sources are almost parallel.

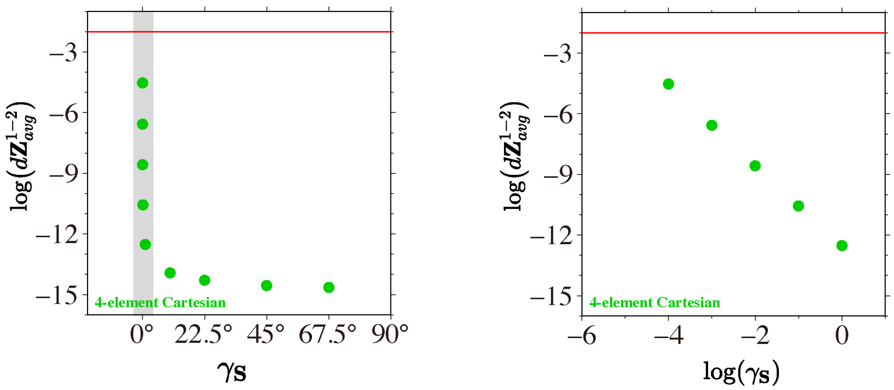

(a) (b)

Figure B3. Dependence of dZ_{avg}^{1-2} on (a) $\gamma_{\mathbf{S}}$ when $\gamma_{\mathbf{S}}$ is between 10^{-5}° and 67.5° and (b) log($\gamma_{\mathbf{S}}$) (corresponding to the shaded zone in (a)) in the entire study region at period of 10,000 sec. Model: Cartesian oceanic model with azimuthal equidistant projection method.

In Case 3, the amplitude of one of two orthogonal sources was chosen to be variable. The source combination is denoted as $\{\hat{\mathbf{S}}_x, a_y\hat{\mathbf{S}}_y\}$, where the amplitude factor a_Y varies between 10^{-5} and 10^{5}. The results, shown in Figure 12, indicate that the Cartesian impedance is independent of the source amplitude.

We summarize the results of the above three cases that the Cartesian impedances calculated from a combination of EM fields generated from two independent sources are unique and independent of the source amplitude and polarization. The source polarization effect in Case 2 can be regarded as a source amplitude effect when the amplitude of one source is very small. However, in Case 3, we confirmed the absence of the source amplitude effect even when the amplitude is either very small or very large. Therefore Case 3 provides a more general examination of this phenomenon.

Acknowledgments

We thank Makoto UYESHIMA for providing an original 3-D spherical modeling code. We thank Ömer Faruk BODUR and Kiyoshi BABA for their comments. We thank Alexander

GRAYVER, Anna KELBERT and two associate editors for their valuable comments and suggestions.

This study was partially supported by Geological Joint Fund of National Natural Science Foundation of China (Key Fund Project, under Grant No. U2344203), National Natural Science Foundation of China (under Grant No. 42474105, 42074079), JSPS KAKENHI (grant #21H01186), Interdisciplinary Project in Ocean Research of Tongji University and the Fundamental Research Funds for the Central Universities, Independent Project of the State Key Laboratory of Marine Geology at Tongji University (under Grant No. MGZ202403), Major Project of China National Petroleum Corporation (under Grant No. 2023ZZ05-05), and Jiangsu Province Carbon Peak Carbon Neutral Technology Innovation Project in China (under Grant No.BE2022034-3).

Open Research

The dataset used in the figures in this study can be accessed on Zenodo (Wan & Utada, 2024).

References

Amante, C., & Eakins, B. W. (2009). ETOPO1 Global Relief Model converted to PanMap layer format. NOAA-National Geophysical Data Center, PANGAEA, doi:10.1594/PANGAEA.769615

Araya, J., Ritter, O., & Brändlein, D. (2013). Long-term variations of magnetotelluric transfer functions in northern Chile. In 25. Schmucker-Weidelt-Kolloquium für Elektromagnetische Tiefenforschung (pp. 124–129).

Baba, K., Utada, H., Goto, T. N., Kasaya, T., Shimizu, H., & Tada, N. (2010). Electrical conductivity imaging of the Philippine Sea upper mantle using seafloor magnetotelluric data. Physics of the Earth and Planetary Interiors, 183(1–2), 44–62. doi:10.1016/j.pepi.2010.09.010

Banks, R. J. (1969). Geomagnetic variations and the electrical conductivity of the upper mantle. Geophysical Journal International, 17(5), 457–487. doi:10.1111/j.1365-246X.1969.tb00252.x

Berdichevsky, M. N. (1999). Marginal notes on Magnetotellurics. Surveys in Geophysics, 20, 341–375. doi:10.1023/A:1006645715819

Berdichevsky, M. N. & Dmitriev, V.I. (1997). On deterministic nature of magnetotelluric impedance, Acta Geophysica Polonica XLV(3), 227–236

Brändlein, D., Lühr, H., & Ritter, O. (2012). Direct penetration of the interplanetary electric field to low geomagnetic latitudes and its effect on magnetotelluric sounding. Journal of Geophysical Research: Space Physics, 117(A11). doi:10.1029/2012JA018008

Cagniard, L. (1953). Basic theory of the magneto-telluric method of geophysical prospecting. Geophysics, 18(3), 605–635. doi:10.1190/1.1437915

Chave, A. D., & Jones, A. G. (Eds.). (2012). The magnetotelluric method: Theory and practice. Cambridge University Press. doi:10.1017/CBO9781139020138

Dmitriev, V. I. & Berdichevsky, M. N. (2002). A generalized Impedance Model. Izestiya, Physics of the Solid Earth, 38(10), 897-903.

Egbert, G. D., & Kelbert, A. (2012). Computational recipes for electromagnetic inverse problems. Geophysical Journal International, 189(1), 251–267. doi:10.1111/j.1365-246X.2011.05347.x

Ernst, T., Nowożyński, K., & Jóźwiak, W. (2020). The reduction of source effect for reliable estimation of geomagnetic transfer functions. Geophysical Journal International, 221(1), 415–430. doi:10.1093/gji/ggaa017

Ernst, T., Nowożyński, K., & Jóźwiak, W. (2022). Source effect impact on the magnetotelluric transfer functions. Annals of Geophysics, 65(1), GM104–GM104. doi:10.4401/ag-8751

Fujita, S., Fujii, I., Endo, A., & Tominaga, H. (2018). Numerical modeling of spatial profiles of geomagnetically induced electric field intensity in and around Japan. Tech Rep Kakioka Magn Observ, 15, 35–50.

Garcia, X., Chave, A. D. & Jones, A. G. (1997). Robust processing of magnetotelluric data from the auroral zone. Journal of geomagnetism and geoelectricity, 49 (11-12), 1451-1468. doi: 10.5636/jgg.49.1451

Garcia, X., & Jones, A. G. (2000). Advances in aspects of the application of magnetotellurics for mineral exploration. In SEG Technical Program Expanded Abstracts 2000 (pp. 1115–1118). Society of Exploration Geophysicists. doi:10.1190/1.1815583

Grayver, A. V., van Driel, M., & Kuvshinov, A. V. (2019). Three-dimensional magnetotelluric modelling in spherical Earth. Geophysical Journal International, 217(1), 532–557. doi:10.1093/gji/ggz030

Grayver, A. V., Munch, F. D., Kuvshinov, A. V., Khan, A., Sabaka, T. J., & Tøffner‐Clausen, L. (2017). Joint inversion of satellite‐detected tidal and magnetospheric signals constrains electrical conductivity and water content of the upper mantle and transition zone. Geophysical research letters, 44(12), 6074–6081. doi:10.1002/2017GL073446

Guzavina, M., Grayver, A., & Kuvshinov, A. (2019). Probing upper mantle electrical conductivity with daily magnetic variations using global-to-local transfer functions. Geophysical Journal International, 219(3), 2125–2147. doi:10.1093/gji/ggz412

Han, Q., & Hu, X. (2023). Three-dimensional Magnetotelluric Modeling in Spherical and Cartesian Coordinate Systems: a Comparative Study. Earth and Planetary Physics, 7, 0–0. doi:10.26464/epp2023048

Han, Q., Hu, X., & Peng, R. (2020). Spherical magnetotelluric modeling based on non-uniform source. Chinese Journal of Geophysics, 63(8), 3154–3166. doi:10.6038/cjg2020N0207

Jiang, W., Duan, J., Doublier, M., Clark, A., Schofield, A., Brodie, R. C., & Goodwin, J. (2022). Application of multiscale magnetotelluric data to mineral exploration: an example from the east Tennant region, Northern Australia. Geophysical Journal International, 229(3), 1628–1645. doi:10.1093/gji/ggac029

Kappler, K. N., Morrison, H. F., & Egbert, G. D. (2010). Long‐term monitoring of ULF electromagnetic fields at Parkfield, California. Journal of Geophysical Research: Solid Earth, 115(B4). doi:10.1029/2009JB006421

Kruglyakov, M., & Kuvshinov, A. (2022). Modelling tippers on a sphere. Geophysical Journal International, 231(2), 737–748. doi:10.1093/gji/ggac199

Kuvshinov, A., & Semenov, A. (2012). Global 3-D imaging of mantle electrical conductivity based on inversion of observatory C-responses—I. An approach and its verification. Geophysical Journal International, 189(3), 1335–1352. doi:10.1111/j.1365-246X.2011.05349.x

Laske, G., & Masters, G. (1997). A Global Digital Map of Sediment Thickness. EOS Transactions American Geophysical Union, 78, F483.

Livelybrooks, D. W., Mareschal, M., Blais, E., & Smith, J. T. (1996). Magnetotelluric delineation of the Trillabelle massive sulfide body in Sudbury, Ontario. Geophysics, 61(4), 971–986. doi:10.1190/1.1444046

Luo, W., Wang, X., Wang, K., Zhang, G., & Li, D. (2019). Three-dimensional forward modeling of the magnetotelluric method in spherical coordinates. Chinese Journal of Geophysics, 62(10), 3885–3897. doi:10.6038/cjg2019M0439

Mackie, R. L., Smith, J. T., & Madden, T. R. (1994). Three - dimensional electromagnetic modeling using finite difference equations: The magnetotelluric example. Radio Science, 29(4), 923–935. doi:10.1029/94RS00326

Mackie, R. L., Madden, T. R., & Wannamaker, P. E. (1993). Three-dimensional magnetotelluric modeling using difference equations; theory and comparisons to integral equation solutions. Geophysics, 58(2), 215–226. doi:10.1190/1.1443407

Matsuno, T., Suetsugu, D., Baba, K., Tada, N., Shimizu, H., Shiobara, H., et al. (2017). Mantle transition zone beneath a normal seafloor in the northwestern Pacific: Electrical conductivity, seismic thickness, and water content. Earth and Planetary Science Letters, 462, 189–198. doi:10.1016/j.epsl.2016.12.045

Newman, G. A., & Alumbaugh, D. L. (2000). Three-dimensional magnetotelluric inversion using non-linear conjugate gradients. Geophysical journal international, 140(2), 410–424. doi:10.1046/j.1365-246x.2000.00007.x

Parkinson, W. D. (1959). Directions of rapid geomagnetic fluctuations. Geophysical Journal International, 2(1), 1–14. doi:10.1111/j.1365-246X.1959.tb05776.x

Price, A. T. (1962). The theory of magnetotelluric methods when the source field is considered. Journal of Geophysical Research, 67(5), 1907–1918. doi:10.1029/JZ067i005p01907

Rosell, O., Martí, A., Marcuello, À., Ledo, J., Queralt, P., Roca, E., & Campanyà, J. (2011). Deep electrical resistivity structure of the northern Gibraltar Arc (western Mediterranean): Evidence of lithospheric slab break ‐ off. Terra Nova, 23(3), 179–186. doi:10.1111/j.1365-3121.2011.00996.x

Schmucker, U. (1970). An introduction to induction anomalies. Journal of Geomagnetism and Geoelectricity, 22(1-2), 9–33. doi:10.5636/jgg.22.9

Schmucker, U. (1987). Substitute conductors for electromagnetic response estimates. Pure and applied geophysics, 125, 341-367. doi: 10.1007/BF00874501

Schmucker, U. (1999a). A spherical harmonic analysis of solar daily variations in the years 1964–1965: response estimates and source fields for global induction—I. Methods. Geophysical Journal International, 136(2), 439–454. doi:10.1046/j.1365-246X.1999.00742.x

Schmucker, U. (1999b). A spherical harmonic analysis of solar daily variations in the years 1964–1965: response estimates and source fields for global induction—II. Results. Geophysical Journal International, 136(2), 455–476. doi:10.1046/j.1365-246X.1999.00743.x

Shimizu, H., Koyama, T., Baba, K., & Utada, H. (2010). Revised 1-D mantle electrical conductivity structure beneath the north Pacific. Geophysical Journal International, 180(3), 1030–1048. doi:10.1111/j.1365-246X.2009.04466.x

Shimizu, H., Yoneda, A., Baba, K., Utada, H., & Palshin, N. A. (2011). Sq effect on the electromagnetic response functions in the period range between 104 and 105 s. Geophysical Journal International, 186(1), 193–206. doi:10.1111/j.1365-246X.2011.05036.x

Simpson, F., & Bahr, K. (2005). Practical magnetotellurics. Cambridge University Press. doi:10.1017/CBO9780511614095

Siripunvaraporn, W., Egbert, G., & Uyeshima, M. (2005). Interpretation of two-dimensional magnetotelluric profile data with three-dimensional inversion: synthetic examples. Geophysical journal international, 160(3), 804–814. doi:10.1111/j.1365-246X.2005.02527.x

Snyder, J. P. (1987). Map projections--A working manual (Vol. 1395). US Government Printing Office. doi:10.3133/pp1395

Srivastava, S. P. (1966). Theory of the magnetotelluric method for a spherical conductor. Geophysical Journal International, 11(4), 373–387. doi:10.1111/j.1365-246X.1966.tb03090.x

Stanley, W. D., Boehl, J. E., Bostick, F. X., & Smith, H. W. (1977). Geothermal significance of magnetotelluric sounding in the eastern Snake River Plain - Yellowstone region. Journal of Geophysical Research, 82(17), 2501–2514. doi:10.1029/JB082i017p02501

Strangway, D. W., Swift, C. M., & Holmer, R. C. (1973). The application of audio-frequency magnetotellurics (AMT) to mineral exploration. Geophysics, 38(6), 1159–1175. doi:10.1190/1.1440402

Tada, N., Baba, K., Siripunvaraporn, W., Uyeshima, M., & Utada, H. (2012). Approximate treatment of seafloor topographic effects in three-dimensional marine magnetotelluric inversion. Earth, planets and space, 64, 1005–1021. doi:10.5047/eps.2012.04.005

Tada, N., Baba, K., & Utada, H. (2014). Three‐dimensional inversion of seafloor magnetotelluric data collected in the Philippine Sea and the western margin of the northwest Pacific Ocean. Geochemistry, Geophysics, Geosystems, 15(7), 2895–2917. doi:10.1002/2014GC005421

Tada, N., Tarits, P., Baba, K., Utada, H., Kasaya, T., & Suetsugu, D. (2016). Electromagnetic evidence for volatile‐rich upwelling beneath the society hotspot, French Polynesia. Geophysical Research Letters, 43(23), 12021–12026. doi:10.1002/2016GL071331

Utada, H. (2018). Plane-wave and flat Earth approximations in natural-source electromagnetic induction studies. Bull Earthq Res Inst Univ Tokyo, 93, 1–14, doi:10.15083/0000051814

Uyeshima, M., & Schultz, A. (2000). Geoelectromagnetic induction in a heterogeneous sphere: a new three-dimensional forward solver using a conservative staggered-grid finite difference method. Geophysical Journal International, 140(3), 636–650. doi:10.1046/j.1365-246X.2000.00051.x

Wan, X., & Utada, H. (2024). Dataset of modeling results. [Data set]. Zenodo. https://doi.org/10.5281/zenodo.10725054

Wannamaker, P. E., Hohmann, G. W., & Ward, S. H. (1984). Magnetotelluric responses of three-dimensional bodies in layered earths. Geophysics, 49(9), 1517–1533. doi:10.1190/1.1441777

Yang, W., Jin, S., Zhang, L., Qu, C., Hu, X., Wei, W., et al. (2020). The three-dimensional resistivity structures of the lithosphere beneath the Qinghai-Tibet Plateau. Chinese Journal of Geophysics, 63(3), 817–827. doi:10.6038/cjg2020N0197

Zhang, H., Egbert, G. D., & Huang, Q. (2023). Constraints on MTZ water content from joint inversion of diurnal variations and magnetospheric signals. Geophysical Research Letters, 50(10), e2023GL102765. doi:10.1029/2023GL102765

Zhang, H., Huang, Q., Zhao, G., Guo, Z., & Chen, Y. J. (2016). Three-dimensional conductivity model of crust and uppermost mantle at the northern Trans North China Orogen: Evidence for a mantle source of Datong volcanoes. Earth and Planetary Science Letters, 453, 182–192. doi:10.1016/j.epsl.2016.08.025